

## Accepted Manuscript

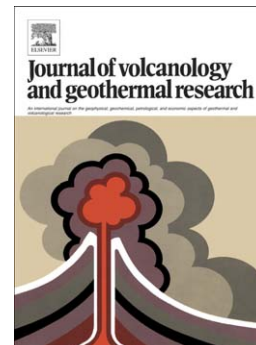
The Masaya Triple Layer: A 2100 year old basaltic multi-episodic Plinian eruption from the Masaya Caldera Complex (Nicaragua)

W. Pérez, A. Freundt, S. Kutterolf, H.-U. Schmincke

PII: S0377-0273(08)00565-9  
DOI: doi: [10.1016/j.jvolgeores.2008.10.015](https://doi.org/10.1016/j.jvolgeores.2008.10.015)  
Reference: VOLGEO 4164

To appear in: *Journal of Volcanology and Geothermal Research*

Received date: 9 January 2008  
Revised date: 17 September 2008  
Accepted date: 16 October 2008



Please cite this article as: Pérez, W., Freundt, A., Kutterolf, S., Schmincke, H.-U., The Masaya Triple Layer: A 2100 year old basaltic multi-episodic Plinian eruption from the Masaya Caldera Complex (Nicaragua), *Journal of Volcanology and Geothermal Research* (2008), doi: [10.1016/j.jvolgeores.2008.10.015](https://doi.org/10.1016/j.jvolgeores.2008.10.015)

This is a PDF file of an unedited manuscript that has been accepted for publication. As a service to our customers we are providing this early version of the manuscript. The manuscript will undergo copyediting, typesetting, and review of the resulting proof before it is published in its final form. Please note that during the production process errors may be discovered which could affect the content, and all legal disclaimers that apply to the journal pertain.

# The Masaya Triple Layer: a 2100 year old basaltic multi-episodic Plinian eruption from the Masaya Caldera Complex (Nicaragua)

W. Pérez\*, A. Freundt, S. Kutterolf, H.-U. Schmincke  
*Sonderforschungsbereich (SFB) 574, University of Kiel  
IFM-GEOMAR, Wischhofstr. 1-3, 21148 Kiel, Germany*

## Abstract

The Masaya Caldera Complex has been the site of three highly explosive basaltic eruptions within the last six thousand years. A Plinian eruption ca. 2 ka ago formed the widespread deposits of the Masaya Triple Layer. We distinguish two facies within the Masaya Triple Layer from each other: La Concepción facies to the south and Managua facies to the northwest. These two facies were previously treated as two separated deposits (La Concepción Tephra and the Masaya Triple Layer of Pérez and Freundt, 2006) because of their distinct regional distribution and internal architectures. However, chemical compositions of bulk rock, matrix and inclusion glasses and mineral phases demonstrate that they are the product of a single basaltic magma batch. Additionally, a marker bed containing fluidal-shaped vesicular lapilli allowed us to make a plausible correlation between the two facies, also supported by consistent lateral changes in lithologic structure and composition, thickness and grain size.

We distinguish 10 main subunits of the Masaya Triple Layer (I to X), with bulk volumes ranging between 0.02 and 0.22 km<sup>3</sup>, adding up to 0.86 km<sup>3</sup> (0.4 km<sup>3</sup> DRE) for the entire deposit. Distal deposits identified in two cores drilled offshore Nicaragua, at a distance of ~170 km from the Masaya Caldera Complex, increase the total tephra volume to 3.4 km<sup>3</sup> or ~1.8 km<sup>3</sup> DRE of erupted basaltic magma.

Isopleth data of five major fallout subunits indicate mass discharges of 10<sup>6</sup> to 10<sup>8</sup> kg/s and eruption columns of 21 to 32 km height, affected by wind speeds of <2 m/s to ~20 m/s which increased during the course of the multi-episodic eruption. Magmatic Plinian events alternated with phreatoplinian eruptions and phreatomagmatic explosions generating surges that typically preceded breaks in activity. While single eruptive episodes lasted for few hours, the entire eruption probable lasted weeks to months. This is indicated by changes in atmospheric conditions and ash-layer surfaces that had become modified during the breaks in activity. The Masaya Triple Layer has allowed to reconstruct in detail how a basaltic Plinian eruption develops in terms of duration, episodicity, and variable access of external water to the conduit, with implications for volcanic hazard assessment.

*Keywords:* Masaya Caldera Complex; Nicaragua; basaltic Plinian eruptions; Tephrostratigraphy; Volcanic hazards

\* Corresponding author. Tel.: +49 431 6002139; fax: +49 431 6002924  
*Email address:* wperez@ifm-geomar.de

## 41 1. Introduction

42  
43 Plinian eruptions of basaltic composition are thought to be rare because basaltic magma  
44 mostly erupts as lava flows and in Strombolian, Hawaiian and Surtseyan fashion when  
45 fragmented. Nevertheless, several examples of widely dispersed basaltic tephra deposits with  
46 Plinian characteristics have been reported during the last two decades (Williams, 1983; Bice,  
47 1985; Wehrmann et al., 2006; Coltelli et al., 1998; McPhie et al., 1990; Dzurisin et al., 1995;  
48 Mastin, 1997; Walker et al., 1984; Sable et al., 2006; Carey et al., 2007; Costantini et al.,  
49 2008). The first account of this type of tephra by Williams (1983) addressed two deposits  
50 thought to have been erupted from the Masaya Caldera Complex in west-central Nicaragua:  
51 the San Judas Formation, later named the Masaya Triple Layer by Bice (1985), and the  
52 Fontana Lapilli, later shown by Wehrmann et al. (2006) to have been derived from a vent  
53 outside Masaya caldera consistent with its age of ca. 60 ka (Kutterolf et al., 2008a).  
54 Pérez and Freundt (2006) have shown that the Masaya caldera produced three widespread  
55 basaltic tephra during the last 6 ka: the San Antonio Tephra, the Masaya Triple Layer, and  
56 the Masaya Tuff, a huge hydroclastic surge deposit covered by the Plinian Ticuantepe Lapilli.  
57 Here we reconstruct the ~2.1 ka Plinian eruption of the Masaya caldera which produced the  
58 Masaya Triple Layer. We distinguish two facies within the Masaya Triple Layer: La  
59 Concepción facies to the south and the Managua facies to the northwest. These two facies  
60 were previously treated as two separated deposits (Pérez and Freundt, 2006) because of their  
61 distinct regional distribution and internal architectures. However, here we use geochemical  
62 and petrographic characteristics to stratigraphically correlate the two facies and to document  
63 their origin from a single basaltic magma batch. We reconstruct the evolution of this long-  
64 lasting multi-episode eruption based on the revised stratigraphy. Such case studies are needed  
65 to better constrain the presently poorly understood processes that force basaltic magmas to  
66 erupt in a Plinian fashion.

67

### 68 1.1 Geologic setting

69

70 Nicaragua is part of the Central American isthmus, where the subduction of the Cocos plate  
71 under the Caribbean Plate at a convergence rate of 70-90 mm/year (Barckhausen et al., 2001;  
72 DeMets, 2001) results in the NW-SE trending Central American Volcanic Arc (CAVA). The  
73 arc volcanoes lie inside the Nicaraguan depression, which is a NW-SE striking flat depression  
74 occupied by Lake Managua and Lake Nicaragua and bordered in the east by the interior  
75 highlands (Fig. 1).

76 The area between the two lakes is the economical and demographic center of the country,  
77 where all large cities are located. The capital Managua is surrounded by several highly  
78 explosive basaltic to rhyolitic volcanic complexes. Major volcanic threats to the Managua  
79 area and its ~1.8 million inhabitants are centered in the Masaya Caldera Complex (Fig. 2), a  
80 volcanic system that repeatedly generated highly explosive basaltic eruptions in the past.

81 The complex consists of a NW-SE elongated caldera 11 km long and 6 km wide, containing  
82 Lake Masaya at the SE rim and the post-collapse volcanic edifice in the western half,  
83 composed of the Masaya and Nindirí cones with their pit craters Masaya, Santiago, Nindirí  
84 and San Pedro (e.g. McBirney, 1956; Rymer et al., 1998). Masaya is one of the most active  
85 volcanoes in Central America and has been the object of several geophysical (e.g. Metaxian et  
86 al., 1997; Lewicki et al., 2003), gas-chemical (e.g., Stoiber et al., 1986; Horrocks et al., 1999;  
87 Duffell et al., 2003) and geochemical (Walker et al., 1993) investigations.

88 Three widespread pyroclastic deposits that originated at Masaya were previously identified:  
89 the Fontana Lapilli, the Masaya Triple Layer or San Judas Formation and the Masaya Tuff or  
90 El Retiro Tuff (Bice, 1985; Williams 1983). We have additionally identified the ca. 6 ka old  
91 San Antonio Tephra (Pérez and Freundt, 2006). A recent detailed study of the Fontana Tephra  
92 by Wehrmann et al. (2006) showed that the source vent of this basaltic Plinian lapilli fallout  
93 did not lie within the Masaya caldera as previously interpreted (Williams, 1983) but a few  
94 kilometers outside to the NW, where it would be part of the older Las Nubes caldera (Girard  
95 and van Wyk de Vries, 2005). The Fontana Tephra age of ~60 ka documented in Kutterolf et  
96 al. (2007, 2008a) supports this result. The ~6 ka San Antonio Tephra is thus the oldest known  
97 product of a basaltic Plinian eruption from the Masaya caldera.

98 The second Plinian eruption at Masaya caldera produced the Masaya Triple Layer (Williams,  
99 1983; Bice, 1985). Re-investigation by Pérez and Freundt (2006) identified two basaltic  
100 tephra deposits overlying the San Antonio Tephra which differ in regional distribution and  
101 internal architecture: the Masaya Triple Layer with a radiocarbon age of 2.1 ka to the NW,  
102 and La Concepción Tephra south of the caldera (Fig. 2). These deposits are the subject of this  
103 paper. The last large eruption from the Masaya caldera produced the Masaya Tuff, a huge  
104 phreatomagmatic pyroclastic surge deposit (Bice, 1985; Williams, 1983). This large-  
105 magnitude Surtseyan eruption terminated in a third Plinian eruption that produced the  
106 widespread Ticuantepe Lapilli, a stratified succession of well-sorted fallouts of vesicular  
107 scoria immediately overlying the Masaya Tuff (Pérez and Freundt, 2006). Kutterolf et al.  
108 (2008a) estimated that this eruption occurred 1.8 ka ago, based on stratigraphic relationships  
109 in offshore sediment cores. Younger products of Masaya volcanism formed the intra-caldera

110 Santiago-Masaya volcanic cone and numerous smaller cones and lava flows within, and partly  
111 outside the caldera (McBirney, 1956; Williams, 1983; Walker et al., 1993).

112

### 113 *1.2 Methodology*

114

115 Our stratigraphic subdivisions and correlations are based on 108 logged outcrops around the  
116 Masaya caldera. Correlations between outcrops are based on lithological criteria as well as  
117 compositional data. Tephra volumes are derived from isopachs maps applying the methods of  
118 Pyle (1989) and Fierstein and Nathenson (1992). Erupted magma masses were calculated by  
119 subtracting the average volume fraction of pores and lithic fragments from the tephra volumes  
120 for each subunit, and then multiplying by a density of 2500 kg/m<sup>3</sup>. Distal thickness data and  
121 isopachs of the total deposit are from marine gravity cores collected offshore Nicaragua  
122 during research cruises M54/2, M66/3a (RV METEOR) and SO173/3 (RV SONNE)  
123 (Kutterolf et al., 2008a). Geometric measures from isopleth maps, based on the average of the  
124 five largest juvenile or lithic clasts, are used to estimate eruption column heights and  
125 discharge rates from comparison with model results of Carey and Sparks (1986), Wilson and  
126 Walker (1987), Woods (1988) and Sparks et al. (1992).

127 Bulk rock major and trace element compositions were determined by X-Ray Fluorescence  
128 (XRF) analyses carried out at IFM-GEOMAR and Inductively Coupled Plasma Mass  
129 Spectrometry (ICP-MS) at the University of Kiel. Mineral, matrix and inclusion glass  
130 compositions were determined by electron microprobe at IFM-GEOMAR. Laser Ablation  
131 Inductively Coupled Plasma Mass Spectrometry (LA-ICP-MS) at Frankfurt University was  
132 used for the trace element chemistry of glass samples.

133

## 134 **2. The Masaya Triple Layer**

135

136 Pérez and Freundt (2006) distinguished two deposits that differ in internal architecture and  
137 regional distribution but occur in the same stratigraphic position: La Concepción Tephra to  
138 the south of Masaya caldera and Masaya Triple Layer to the northwest and across Managua  
139 city (Fig. 2). Here, we re-name these deposits as La Concepción facies and Managua facies,  
140 respectively, while applying the name Masaya Triple Layer (MTL) to the entire deposit.

141 Numerous exposures of MTL exist to the NW and S of Masaya caldera, but no trace was  
142 found in the lowlands NE of the caldera although stratigraphically underlying and overlying  
143 units do occur, as well as on the mountainous Las Sierras ridge to the SW where strong

144 erosion has removed younger deposits (Fig. 2). The MTL is separated from the underlying  
145 San Antonio Tephra by a paleosol and an erosional unconformity. A yellowish massive  
146 reworked tuffaceous deposit separates the MTL from the overlying Chiltepe Tephra in the  
147 Managua area while the MTL is directly overlain by the Masaya Tuff in the south, with a  
148 locally intervening erosional unconformity.

149 Both facies of the MTL consist of well-sorted black lapilli beds, coarse ash layers and grayish  
150 indurated tuffs, some with desiccation cracks at the top. The well-sorted layers consist mostly  
151 of juvenile scoria lapilli to coarse-ash and minor (~1-3 vol. %) lithic fragments mainly of  
152 basaltic lava and rare gabbro. The scoria fragments vary from highly vesicular (up to 80 vol.  
153 % vesicles) to dense juvenile lapilli (<5 vol. % vesicles; using the vesicularity index of  
154 Houghton and Wilson, 1989). The matrix of the scoriae varies from sideromelane with  
155 abundant round vesicles through dark brown to black tachylite with rare irregularly shaped  
156 vesicles (Fig. 3). Phenocrysts are mainly plagioclase with abundant melt inclusions and minor  
157 olivine and clinopyroxene; groundmass microlites are plagioclase and olivine. The bulk-rock  
158 composition is basaltic (50.2-51 wt% SiO<sub>2</sub> and 3.5-4.0 wt% alkalis; Fig. 4).

159

### 160 *2.1 La Concepción facies*

161

162 **La Concepción facies (LCF)** is composed of 17 layers (B0-B16) of well-sorted scoria lapilli  
163 to coarse-ash intercalated with tuffs (Pérez and Freundt, 2006). The upper contact of the  
164 deposit is variably eroded. At some localities it is overlain by a thick overburden of a clayey  
165 sediment, while at other places it is separated from the Masaya Tuff by a deeply incised  
166 erosional unconformity.

167 Most exposures show the succession from B1 to B11 and part of B12 but only a few outcrops  
168 show the complete sequence shown in figure 5. The lowermost layer B0 crops out only in  
169 three exposures <6 km south of the caldera rim and consist of two basal fine ash layers and a  
170 cemented accretionary lapilli-bearing tuff at the top containing hydrothermally altered lithic  
171 clasts and plant remains.

172 Subunit B5 the thickest lapilli layer of the LCF and most distinctive by being composed of  
173 fluidal-textured achnelith lapilli and ash (Fig. 6). Hence it is a useful marker bed in all  
174 outcrops. The total thickness of B5 decreases from 115 cm at 1 km south from the vent to 12  
175 cm at 10 km, where it appears as a single thin layer of achnelith-shaped fine lapilli. In  
176 proximal sections, where the well-sorted, black lapilli fallout is vaguely stratified by vertically  
177 alternating grain size and interrupted by a thin light yellowish layer of fine ash, we distinguish

178 5 levels from bottom to top: **[a]** a highly vesicular, glassy, faintly laminated, moderately well-  
179 sorted lapilli layer with minor amount of juvenile ash and very few lithics. Most of the  
180 juvenile fragments have elongated or contorted shapes, **[b]** is a yellowish fine ash layer  
181 commonly 1 cm thick but reaching 4 cm at 1 km from the caldera rim. **[c]** is the thickest level  
182 reaching 90 cm in the proximal areas. The juvenile particles are similar to [a] but grain size is  
183 larger, size-sorting is better particularly at the top, and the content of lithic fragments is  
184 slightly higher (~1 vol. %). The base of this layer is weakly stratified and consists of fine  
185 lapilli to coarse ash. **[d]** is a weakly stratified medium-ash layer of glassy scoria that is  
186 slightly cemented and **[e]** is a scoria lapilli layer similar to [a].

187 The tuff triplet B6, B8, B10 are also characteristic of the LCF and they thin rapidly  
188 southwards away the caldera rim (Fig. 7). The grayish indurated B6 tuff is in proximal  
189 exposures composed of a lower fine-grained part with accretionary lapilli and an overlying  
190 cross-bedded layer of fine lapilli to coarse ash. In medial exposures, this unit is condensed to  
191 an indurated tuff with vesicular lapilli at the bottom and a laminated medium to fine ash layer  
192 with scarce accretionary lapilli at the top.

193 B8 is an indurated tuff up to 60 cm thick at proximal locations (~1 km from the vent). Its  
194 lower part is cross-bedded with dune structures of alternating coarse and fine lapilli layers. In  
195 the medial facies, B8 is a 20 cm thick tuff with a 1 cm yellowish fine ash at the bottom,  
196 overlain by an indurated fine tuff with accretionary lapilli and dispersed glassy scoria clasts.  
197 A strongly cemented light gray fine tuff layer forms the top.

198 B10 is proximally stratified, poorly-sorted, coarse ash with dispersed lapilli at the base, fine to  
199 medium ash with dune structures in the middle portion, and a highly indurated tuff at the top.  
200 At medial exposures S or SE from the caldera rim, B10 consists of an indurated grayish cross-  
201 bedded tuff with coarse ash and fine lapilli at the bottom and a fine ash with accretionary  
202 lapilli at the top (Fig. 7). At distal exposures to the S and SW, it appears as a thin indurated  
203 tuff with accretionary lapilli, slightly laminated at the bottom.

204

## 205 2.2 Managua facies

206

207 The Managua facies of the MTL north and northwest of the caldera consists of 10 layers (C1  
208 to C10), 7 of them are scoria lapilli to coarse-ash layers and the others are tuffs (Fig. 8, table  
209 2). No outcrops could be found close to the Masaya caldera rim, the most proximal are those  
210 located at 7 to 7.5 km distance, along the road from San Antonio Sur to El Crucero, where the

211 facies reaches its maximum observed thickness. Here we describe four characteristic layers of  
212 the MF, brief descriptions of all subunits are given in table 2.

213 Layer C2 is a well-sorted fine lapilli layer of highly vesicular scoria containing <1 vol. % of  
214 lithic fragments and reaching a maximum thickness of 5 cm. Towards >13 km to the NW of  
215 Masaya caldera, C2 grades into a ~1 cm thick black ash layer. C2 is a useful marker bed due  
216 to the fluidal morphology and high vesicularity of the glassy scoria.

217 At the most proximal exposures, C3 consists of several intercalated tuff and lapilli beds.  
218 Three main layers can be distinguished across the medial range: a fine yellowish indurated  
219 tuff with leaf molds at the base, a moderately well-sorted normal-graded layer of scoria lapilli  
220 and a relatively large fraction of lithic angular dense aphyric basaltic lava fragments (~5-15  
221 vol. %, some hydrothermally altered) in a matrix of coarse ash (~30 vol. %), and a topmost  
222 thin hard tuff with desiccation cracks at the surface. All particles are coated with brownish  
223 fine ash. Plant remains from the basal tuff have been radiocarbon dated to  $2,120 \pm 120$  years  
224 BP (Pérez and Freundt, 2006).

225 C7 is >40 cm thick yellowish tuff with abundant accretionary lapilli (diameters 2-10 mm) and  
226 scarce armored lapilli, is stratified by horizons enriched in lapilli or coarse-ash fragments, or  
227 accretionary lapilli. The quality of this texture varies between outcrops from apparently  
228 massive to well bedded; different degrees of induration locally emphasize the bedding.

229 C10 is the thickest and coarsest lapilli layer of the Managua facies, with a maximum observed  
230 thickness of 36 cm at 10 km to the NW of the caldera, decreasing to 3 cm near Ciudad  
231 Sandino (~25 km from the Masaya caldera). This well-sorted deposit of scoria lapilli is  
232 typically reversely graded at medial exposures but grading patterns are more variable at  
233 proximal outcrops, with two reversely graded horizons or symmetrical grading with largest  
234 grain size near the center.

235

### 236 **3. Correlation between the facies**

237

238 The different internal architectures of La Concepción and Managua facies do not allow to  
239 easily correlate individual layers, especially because there are no linking outcrops southwest  
240 and northeast the caldera. Yet both facies occur in the same stratigraphic position (Pérez and  
241 Freundt, 2006). Here we use chemical compositions to show that they are derived from the  
242 same magma batch. Based on that supposition, we then use petrographic and lithologic  
243 criteria to propose a layer-by-layer correlation.

244



### 245 3.1 Chemical compositions

246

247 A detailed stratigraphic sampling of several exposures at variable distances and directions  
248 from the Masaya caldera allowed us to compare the chemical compositions of bulk rock,  
249 matrix and inclusion glasses and mineral phases. Both, La Concepción and the Managua  
250 facies, are tholeiitic basalts and have completely overlapping bulk rock major and trace  
251 element compositions (Figs. 4, 9). These compositions are the least evolved of, and hence  
252 distinct from, the compositions of the other mafic tephras produced by the Masaya system  
253 (Fig. 4). They also differ in composition and by their young age from the Las Sierras  
254 Formation tephras.

255 The basaltic-andesitic compositions of the matrix glasses from both facies overlap completely  
256 in both major and trace elements (Fig. 9a, b); their displacement from whole-rock  
257 compositions largely reflects the abundance of plagioclase crystals in the latter. Moreover, the  
258 basaltic to basaltic andesitic glass inclusions, mostly hosted in plagioclase phenocrysts, show  
259 no compositional differences between the facies (Fig. 9c).

260 Likewise, the minerals in the scoriae of both facies are compositionally identical (Fig. 9d).  
261 The dominant mineral phase is calcic plagioclase ranging from An<sub>73</sub> to An<sub>89</sub>, and the  
262 microlites in the groundmass are at the calcic end of this range. The olivines of the LCF have  
263 Mg-numbers between 0.72-0.74, while those of the MF have a wider range of 0.70-0.82.  
264 Augites of Wo<sub>39-41</sub> En<sub>45-48</sub> Fs<sub>11-15</sub> compositions with 0.47-0.57 wt% TiO<sub>2</sub> and 2.2 to 3.9 wt%  
265 Al<sub>2</sub>O<sub>3</sub> are the same in both facies.

266 All these chemical criteria demonstrate that the two facies represent the deposit of one  
267 eruption of a single basaltic magma. Vertical changes show that this magma was somewhat  
268 heterogeneous in composition. Bulk-rock scoria compositions slightly increase in Al<sub>2</sub>O<sub>3</sub> and  
269 decrease in TiO<sub>2</sub>, Ba, FeO and alkalis upward through the deposit. An-contents of plagioclase  
270 phenocrysts increase upward and layers C1, C4 and C10 contain olivines with the widest  
271 range in Mg-numbers. The vertical compositional changes, however, are too subtle to be used  
272 for a detailed correlation of the two facies successions. Correlations must thus be based on  
273 lithologic characteristics such as scoria texture.

274

### 275 3.2 Proposed correlation

276

277 Two well-sorted layers, B5 of the LCF and C2 of the MF, are prominent in their respective  
278 facies because they consist entirely of highly vesicular, fluidally-textured elongate achneliths

279 (see Fig. 7). Masaya volcano has repeatedly produced such scoria particles in eruptions  
280 ranging from the ~6 ka San Antonio Tephra (Pérez and Freundt, 2006) to the recent products  
281 of active Santiago crater. In the MTL, however, their dominant occurrence is limited to two  
282 layers. We therefore use the correlation B5=C2 as a starting point to merge the layers of the  
283 two facies into 10 correlated depositional units (I-X) based on similar lithologic and  
284 petrographic properties. The combined stratigraphy agrees with the overall upward increase in  
285 less vesicular scoria particles and hydrothermally altered lithics observed in both facies. Each  
286 new subunit has been checked for consistency of the resulting areal thickness and grain-size  
287 distributions. The most plausible correlation scheme between La Concepción and Managua  
288 facies is illustrated in figure 10. The major well-sorted lapilli fallout layers of both facies are  
289 correlated resulting in subunits II (B5, C2), IV (B9, C4), VI (B11, C6), VIII (B14, C8) and X  
290 (B16, C10). The areal distributions of these fallouts and their volcanological significance are  
291 discussed below. First, we summarize the implications for the tuff deposits.

292 Subunit I consists of layers B0 to B4 which thin to the NW and merge into layer C1, which  
293 contains a horizon rich in plant material resembling B2. The opening phase of the MTL  
294 eruption represented by subunit I began with minor phreatomagmatic ash fallouts (B0)  
295 followed by a more intense eruption emplacing the first lapilli fallout B1, which is interrupted  
296 by a weak ash surge (B2) before a weaker column is re-established (fallout B3) that finally  
297 collapsed when a wet surge (B4) was erupted. The distal fallout of B1 and B3 is combined in  
298 layer C1.

299 Subunit III includes the two surge layers B6 and B8, which are separated by the lapilli fallout  
300 B7. This tri-partite structure is preserved in a condensed fashion in the distal layer C3 in the  
301 NW.

302 Subunit V combines the tuffs B10 and C5 and represents the deposit of a major, energetic wet  
303 surge event.

304 Subunit VII is a surge deposit (B12) capped by a tuff rich in accretionary lapilli (B13) that  
305 forms a single thick accretionary-lapilli-rich tuff (C7) distally in the NW, probably the deposit  
306 of wind-driven ash clouds of the surges.

307 Subunit IX (B15, C9) has characteristics of an ash-rich surge that –in contrast to the earlier  
308 surges– expanded more strongly to the NW and was weaker to the S. The deposit is  
309 everywhere capped by an indurated thin fine-ash layer, the final wet fallout from the surge  
310 cloud.

311 Desiccation cracks at the tops of subunits III, V and IX indicate significant breaks in the  
312 eruptive activity and dry warm weather conditions as also supported by the absence of

313 erosion. The areal thickness distribution of the tuff subunits is controlled by topography, as  
314 shown by the isopach maps of subunits V, VII and IX (Fig. 11). However, the major  
315 pyroclastic surges were not restricted to low flat areas but surmounted the Las Sierras hills  
316 west of the Masaya caldera to produce significant deposits on their lee flanks.

317

#### 318 **4. The major fallout deposits**

319

320 Preliminary estimates of eruption parameters for the entire deposit, based on separate  
321 treatment of the LCF and MF fallout data, have been given by Pérez and Freundt (2006) and  
322 Kutterolf et al. (2007). Here we re-interpret the data using isopach and isopleth maps of the  
323 major fallout subunits defined by the proposed correlation between the facies. These isopach  
324 and isopleth maps remain poorly constrained southwest and northeast of the caldera where  
325 MTL outcrops are lacking. Thickness data for subunit VII to X to the south are scarce due to  
326 post-emplacement erosion of the top of the MTL. Vent positions cannot be determined  
327 precisely because proximal outcrops are restricted to the area close to the southern caldera  
328 rim. Nevertheless, all isopach maps indicate a vent inside the Masaya caldera, possibly  
329 beneath the modern Masaya intra-caldera cone.

330

##### 331 *4.1 Dispersal characteristics*

332

333 The isopach maps for the correlated fallout subunits I, III, IV, VI, and X all show a dispersion  
334 towards the NW, in direction to Managua city (Fig. 11). In detail, however, there are  
335 differences in the isopach elongation and axis orientation between subunits, indicating  
336 changing wind conditions. For example, the concentric circular pattern of subunit II isopachs  
337 indicates calm conditions whereas a strong wind blowing toward the NW generated the  
338 elongated isopachs of subunit IV.

339 All major fallout subunits show a gradual decay in thickness with distance, typical for  
340 Plinian-type deposits (Fig. 12). Minor variations in thickness decrease between the subunits  
341 reflect variations in eruption intensity. Moreover, values of thickness half-distance ( $b_t$ ) and  
342 clast half-distance ( $b_c$ ) for these deposits of 2.6-3.9 km and 6-18 km, respectively, are in the  
343 ranges typical for Plinian eruptions (Pyle, 1989).

344 The frequent interruption of the Plinian-type eruptions by phreatomagmatic, typically surge-  
345 producing events, suggests that external water affected all eruptive pulses but to variable  
346 extent. Subunits II and IV are relatively lithic-poor, well-sorted, and contain a large fraction

347 of highly vesicular scoria lapilli. We interpret these as mainly magmatic Plinian eruptions  
348 (while noting that the presence of partially quenched lapilli indicates access of some water to  
349 the conduit). On the other hand, subunits III, VI and X are moderately sorted ( $\sigma > 1.5$ ), more  
350 lithic-rich and most of the scoriae are poorly vesicular; moreover, scoria lapilli in subunit III  
351 are ash-coated and proximally intercalated with tuff layers. We interpret these eruptive events  
352 as Phreatoplinian since they were clearly more strongly affected by magma-water interaction.  
353 Fallout subunit VIII shows locally variable faint parallel or cross-bedding; this may be due to  
354 surge-blast expansion contemporaneous with fallout emplacement but may also have been  
355 caused by strong near-surface wind.

356

#### 357 *4.2 Eruption column heights and wind speed*

358

359 We use downwind and crosswind ranges obtained from isopleth maps of maximum juvenile  
360 (MP) and lithic fragments (ML) of the fallout subunits II, III, IV, VI, VIII and X for  
361 comparison with eruption-column modeling results of Carey and Sparks (1986) to estimate  
362 eruption column heights and wind speeds (Fig. 13). The resulting overall range in column  
363 heights is 15 to 32 km. The best-constrained values suggest 22-24 km for subunit II, 22-28 km  
364 for subunit III, 21-23 km for subunits IV and VI, and 26-32 km for subunit X. Magma mass  
365 discharge rates can be estimated from eruption column heights by comparison with the model  
366 results of Woods (1988). Resulting discharge rates for the fallout subunits lie between  $10^7$  to  
367  $10^8$  kg/s (Fig. 14), with subunit X having the highest discharge close to  $10^8$  kg/s.

368 Estimated wind speeds are  $< 2$  m/s for subunit II in agreement with its concentric circular  
369 isopach and isopleth patterns, around 10 m/s for subunits III, IV and VI, and  $\sim 20$  m/s for the  
370 topmost subunit X. These differences reflect changes in wind strength both with time and  
371 with height in the atmosphere. The data in figure 13 suggest that the coarser material  
372 emplaced within 5-10 km from vent never reached the stratosphere and that its dispersal was  
373 controlled by tropospheric winds. Different tropospheric and stratospheric wind directions  
374 and strengths caused bends in dispersal axes of some fallout deposits. The isopach pattern of  
375 subunit III extends proximally westward before turning toward NW, and subunit VI  
376 proximally extends to the S while the main fan is directed to the NW. On the other hand, the  
377 distal fallouts from wind-driven surge clouds all extend to the NW; this may suggest that  
378 near-surface wind directions were more constant than those in the higher troposphere.  
379 Present-day winds at the surface and in the stratosphere (cf. Kutterolf et al., 2007) blow  
380 westward throughout the year but change in the upper troposphere from northeastern

381 directions during the dry season to southwestern directions during the rainy season. If similar  
382 conditions prevailed 2 ka ago, subunits V and VI, with proximally southerly dispersal, would  
383 have been erupted during the rainy season. On the other hand, desiccation cracks at the  
384 surface of subunits III, V and IX suggest dry and hot weather. The different transport and  
385 wind conditions, indications of breaks in volcanic activity, as well as the changes in eruption  
386 style support that the MTL eruption consisted of numerous separate episodes that occurred  
387 over an extended period of time, possibly several months. Individual fallout episodes may  
388 have lasted 1-3 hours judging from mass discharge rates and erupted masses discussed in the  
389 next section.

390

#### 391 *4.3 Volume*

392

393 The subunit tephra volumes range from 0.02 to 0.22 km<sup>3</sup> (Table 3) and are equivalent to  
394 erupted magma masses between 10<sup>10</sup> and 10<sup>11</sup> kg. The fallout subunits II, III and X represent  
395 the eruptive episodes with the largest magnitudes. The added-up total tephra volume of the  
396 Masaya Triple Layer is 0.86 km<sup>3</sup>, a minimum estimate based on land outcrops.

397 Two ash layers found in sediment cores drilled at the continental slope ~170 km away from  
398 the Masaya caldera have been correlated with the Masaya Triple Layer based on their  
399 identical major and trace element chemical compositions, as well as other criteria, e.g.  
400 stratigraphic position of other dated and correlated ash layers in the core, mineral assemblages  
401 and texture of the glass shards (Kutterolf et al., 2008a). The ash layer in core M54/2 is 6 cm  
402 thick, the one in core SO173/3-18 4 cm (Fig. 15). These data imply a much flatter thickness  
403 decay distally than on land (see inset in Fig. 12) and hence yield a significantly increased  
404 tephra volume of the MTL of 3.4 km<sup>3</sup> (~1.8 km<sup>3</sup> DRE, after Kutterolf et al., 2008b). The  
405 additional distal volume must be attributed to the major fallout events because the intercalated  
406 tuffs from phreatomagmatic pulses do not reach that far.

407 The land isopachs show a major dispersion axis towards the northwest, whereas the distal  
408 isopachs suggest transport to the west, reflecting wind directions changing with height. This  
409 decoupling in transport direction has been reported for several eruptions around the world  
410 (e.g. Sarna-Wojcicki et al., 1981; van den Bogaard and Schmincke, 1984; Adams et al.,  
411 2001). A similar pattern to that of the MTL is exhibited by the 25 ka Upper Apoyo Tephra  
412 (Kutterolf et al., 2007, 2008a), coinciding with stratospheric winds to the west above 27 km  
413 height and lower tropospheric winds to the west-northwest (see Kutterolf et al., 2007).

414

## 415 5. The Masaya Triple Layer eruption

416

417 Two facies of volcanic deposits that occur in different areas to the N and S of Masaya caldera  
418 at the same stratigraphic position have identical magmatic compositions and are thus the  
419 deposit of a single eruption although they differ in internal architectures. La Concepción  
420 facies of the Masaya Triple Layer is the more proximal facies of the eruption south of the  
421 caldera, deposited in an area where fallout was still controlled by tropospheric rather than  
422 stratospheric winds and where a rougher topography controlled the flow paths of the surges.  
423 The Managua facies of the MTL, on the other hand, includes the medial and distal deposits in  
424 the direction of fallout dispersion by stratospheric wind and of fine-ash fallout from surge-  
425 related ash-clouds driven by near-surface wind. Using the proposed correlation between the  
426 two facies (Fig. 10), we summarize the evolution of the MTL eruption in figure 16. The MTL  
427 eruption consisted of many episodes separated by time breaks sufficiently long for  
428 atmospheric wind conditions to change and for desiccation cracks to form on the surface of  
429 ash emplaced wet. The eruption style varied between phreatomagmatic explosions and  
430 sustained Plinian and Phreatoplinian eruption columns that reached high into the stratosphere.  
431 The eruption started with phreatomagmatic precursor activity, producing ash fall (**B0, subunit**  
432 **I**) limited to proximal areas south of the caldera. The first main eruptive episode began with  
433 minor phreatomagmatic fallout (**B1**) and minor surges that ripped off vegetation, then became  
434 more magmatic with fallout **B3** but terminated with another phreatomagmatic eruption of ash  
435 fallout (**B4**). Opening and widening of the vent probably contributed to the relatively high  
436 lithic contents of these deposits. The next episode (**subunit II**) was the first major magmatic  
437 Plinian eruption that evacuated  $0.038 \text{ km}^3$  of fresh non-degassed magma and formed an  
438 eruption column of 22-24 km height lasting for ~1 h (derived by dividing DRE mass by mass  
439 flux). Vertical grain-size variations suggest the eruption to have fluctuated in intensity while  
440 fallout dispersal was concentric under calm wind conditions. The characteristic fluidal shapes  
441 of the lapilli (achneliths) indicate eruption of a hot low-viscosity magma that remained  
442 unaffected by contact with external water.

443 The next episode (**subunit III**) was mostly phreatomagmatic, forming surges that destroyed  
444 and carried along the vegetation. Intermittent ~22-28 km high eruption columns were unstable  
445 and collapsed to form minor surges. A break in activity (desiccation cracks on tuff surface)  
446 preceded the second major Plinian eruption (**subunit IV**), during which water access to the  
447 conduit was largely inhibited and which took a couple of hours to eject  $0.025 \text{ km}^3$  of magma  
448 in an eruption column rising to 21-23 km. When water regained access to the conduit, the

449 following phreatomagmatic episode (**subunit V**) formed surges that flowed mainly towards  
450 the south, whereas their ash-clouds were driven towards the NW by near-surface wind.  
451 Desiccation cracks at the top of the tuff indicate another major break after this episode. The  
452 MTL eruption started again with a Phreatoplinian eruption column (**subunit VI**) of similar  
453 dimensions than during the subunit-IV episode but more strongly affected by external water  
454 as evidenced by the higher fraction of hydrothermally altered lithics and poorly vesicular  
455 scoriae. Increasing flux of water into the conduit then resulted in the largest phreatomagmatic  
456 episode of the entire eruption (**subunit VII**) that produced thick surge deposits to the S and  
457 associated ash-cloud deposits rich in accretionary lapilli to the NW. A low-intensity  
458 phreatomagmatic episode (**subunit VIII**) followed and formed a fine-grained, relatively well-  
459 sorted deposit with faint cross bedding, suggesting fallout with a minor lateral transport  
460 component possibly from a low drifting ash cloud. The next episode had regained higher  
461 intensity and mainly generated phreatomagmatic surges of widespread distribution (**subunit**  
462 **IX**). Another significant break in activity allowed for desiccation cracks to form on the  
463 surface of this deposit. The terminal episode of the MTL eruption (**subunit X**) was the most  
464 vigorous event with a 26-32 km high Phreatoplinian eruption column fed by a relative high  
465 magma discharge rate. The fallout dispersal of the  $\sim 0.1 \text{ km}^3$  of magma was mainly controlled  
466 by strong stratospheric winds. The nature of the juvenile fragments and the high fraction of  
467 lithic clasts, some hydrothermally altered, suggest intense magma-water interaction.

468

## 469 **6. Conclusions**

470

471 The Masaya Triple Layer provides an example of the complex evolution of a basaltic Plinian  
472 eruption. The repeated alternation between clearly phreatomagmatic tuffs and fallout deposits  
473 ranging from “magmatic” to “phreatomagmatic” characteristics suggests that external water to  
474 some extent controlled the eruptive style of all eruption events such that even the explosivity  
475 of the apparently magmatic events may have been increased by water vaporization. Peaks in  
476 water access generating phreatomagmatic explosions were followed by breaks in eruptive  
477 activity (desiccation cracks at the top of tuff layers), perhaps due to exhaustion of the water  
478 reservoir and the necessity for the magma system to build up pressure for the next eruption.  
479 Therefore, the MTL Plinian eruption was not only unsteady but multi-episodic, lasting for  
480 weeks or months with intervening extended periods of inactivity. This is a critical issue for  
481 hazard assessments, because major break during an eruption may be mistaken for the end of

482 the eruption while, as shown for the MTL eruption, the most powerful event may still be  
483 coming.

484

#### 485 **Acknowledgments**

486

487 This publication is contribution No. 140 of the Sonderforschungsbereich (SFB) 574 “Volatiles  
488 and Fluids in Subduction Zones” at Kiel University. This work was part of W. Pérez PhD  
489 thesis, which was partly supported by the German Academic Exchange Service (DAAD). We  
490 thank the Instituto Nicaragüense de Estudios Territoriales (INETER) for logistic support in  
491 the field. S. da Silva and J. Fierstein provided constructive revisions that improved this paper.

492

493

#### 494 **References**

495

496 Adams, N.K., de Silva, S.L., Self, S., Salas, G., Schubring, S., Permenter, J.L., Arbesman, K.,  
497 2001. The physical Volcanology of the 1600 eruption of Huaynaputina, southern Peru.  
498 *Bull. Volcanol.* 62, 493-518.

499 Barckhausen, U., Ranero, C.R., von Huene, R., Cande, S.C. and Roeser, H.A., 2001. Revised  
500 tectonic boundaries in the Cocos plate off Costa Rica: Implications for the  
501 segmentation of the convergent margin and for plate tectonic models. *J. Geophys. Res.*  
502 106, 19207-19220.

503 Bice, D.C., 1985. Quaternary volcanic stratigraphy of Managua, Nicaragua: Correlation and  
504 source assignment for multiple overlapping plinian deposits. *Geol. Soc. Amer. Bull.*  
505 96, 553-566.

506 Carey, S., Sparks, R.S.J., 1986. Quantitative models of fallout and dispersal of tephra from  
507 volcanic eruption columns. *Bull. Volcanol.* 48, 109-125.

508 Carey, R., Houghton, B.F., Sable, J.E., Wilson, C.J.N., 2007. Contrasting grain size and  
509 componentry in complex proximal deposits of the 1886 Tarawera basaltic Plinian  
510 eruption. *Bull. Volcanol.* 69, 903-926.

511 Coltelli, M., Del Carlo, P., Vezzoli, L., 1998. Discovery of a Plinian basaltic eruption of  
512 Roman age at Etna volcano, Italy. *Geology* 26, 1095-1098.

513 Costantini, L., Bonadonna, C., Houghton, B.F., Wehrmann, H., 2008. New physical  
514 characterization of the Fontana Lapilli basaltic Plinian eruption, Nicaragua. *Bull.*  
515 *Volcanol* (in press).

516 DeMets, C., 2001. A new estimate for present-day Cocos-Caribbean plate motion:  
517 Implications for slip along the Central American volcanic arc. *Geophys. Res. Lett.* 28,  
518 4043-4046.

519 Duffell, H.J., McGonigle, A.J.S., Burton, M.R., Oppenheimer, C., Pyle, D.M., and Galle, B.,  
520 2003. Changes in gas composition prior to a minor explosive eruption at Masaya  
521 volcano, Nicaragua. *J. Volcanol. Geotherm. Res.* 126, 327-339. doi:10.1016/S0377-  
522 0273(03)00156-2.

523 Dzurisin, D., Lockwood, J.P., Casadevall, T.J. and Meyer, R., 1995. The Uwekahuna Ash  
524 Member of the Puna Basalt: product of a violent phreatomagmatic eruptions at Kilauea  
525 volcano, Hawaii, between 2800 and 2100 14C years ago. *J. Volcanol. Geotherm. Res.*  
526 66, 163-184.



- 527 Fierstein, J., Nathenson, M., 1992. Another look at the calculation of fallout tephra volumes.  
528 Bull. Volcanol. 54, 156-167.
- 529 Girard, G., van Wyk de Vries, B., 2005. The Managua Graben and Las Sierras-Masaya  
530 volcanic complex (Nicaragua); pull-apart localization by an intrusive complex: results  
531 from analogue modeling. J. Volcanol. Geotherm. Res. 144, 37-57.
- 532 Houghton, B.F., Wilson, C.J.N., 1989. A vesicularity index for pyroclastic deposits. Bull.  
533 Volcanol. 51, 451-462.
- 534 Houghton, B.F., Wilson, C.J.N. and Pyle, D.M., 2000. Pyroclastic fall deposits. In: H.  
535 Sigurdsson, B.F. Houghton, S. McNutt, H. Rymer, J. Stix (Editors), Encyclopedia of  
536 volcanoes, Academic Press, San Diego, pp 555–570.
- 537 Horrocks, L., Burton, M., Francis, P., Oppenheimer, C., 1999. Stable gas plume composition  
538 measured by OP-FTIR spectroscopy at Masaya volcano, Nicaragua, 1998-1999.  
539 Geophys. Res. Lett. 26, 3497-3500.
- 540 Kutterolf, S., Freundt, A., Pérez, W., Mörz, T., Schacht, U., Wehrmann, H., Schmincke, H.-  
541 U., 2008a. The Pacific offshore record of Plinian arc volcanism in Central America: 1.  
542 Along-arc correlations. Geochemistry, Geophysics, Geosystems 9.  
543 doi:10.1029/2007GC001631
- 544 Kutterolf, S., Freundt, A., Pérez, W., 2008b. The Pacific offshore record of Plinian arc  
545 volcanism in Central America: 2. Tephra volumes and erupted masses. Geochemistry,  
546 Geophysics, Geosystems 9. doi:10.1029/2007GC001791.
- 547 Kutterolf, S., Freundt, A., Pérez, W., Wehrmann, H. and Schmincke, H.-U., 2007. Late  
548 Pleistocene to Holocene temporal succession and magnitudes of highly-explosive  
549 volcanic eruptions in west-central Nicaragua. J. Volcanol. Geotherm. Res. 163, 55-82.
- 550 Lewicki, J.L., Connor, C., St-Amand, K., Stix, J., Spinner W., 2003. Self-potential, soil CO<sub>2</sub>  
551 flux, and temperature on Masaya volcano, Nicaragua. Geophys. Res. Lett. 30, 1817.  
552 doi:10.1029/2003GL017731
- 553 Mastin, L.G., 1997. Evidence for water influx from a caldera lake during the explosive  
554 hydromagmatic eruption of 1790, Kilauea volcano, Hawaii. J. Geophys. Res. 102,  
555 20093-20109.
- 556 McBirney, A.R., 1956. The Nicaraguan volcano Masaya and its caldera. Amer. Geophys.  
557 Union Transactions 37, 83-96.
- 558 McPhie, J., Walker, G.P.L., Christiansen, R.L., 1990. Phreatomagmatic and phreatic fall and  
559 surge deposits from explosions at Kilauea volcano, Hawaii, 1790 A.D.: Keanakakoi  
560 Ash Member. Bull. Volcanol. 52, 334-354.
- 561 Métaxian, J.-Ph., Lesage, Ph., Dorel, J., 1997. The permanent tremor of Masaya volcano,  
562 Nicaragua: Wave field analysis and source location. J. Geophys. Res. 102, 22,529-  
563 22,545.
- 564 Pérez, W., Freundt, A., 2006. The youngest highly explosive basaltic eruptions from Masaya  
565 Caldera (Nicaragua). In: W.I. Rose, G.J.S. Bluth, M.J. Carr, J.W. Ewert, L.C. Patino,  
566 J.W. Vallance (Editors), Volcanic hazards in Central America. Geol. Soc. Am. Spec.  
567 Pap. 412, pp 189-207.
- 568 Pyle, D.M., 1989. The thickness, volume and grain-size of tephra fall deposits. Bull.  
569 Volcanol. 51, 1-15.
- 570 Rymer, H., van Wyk de Vries, B., Stix, J., Williams-Jones, G., 1998. Pit crater structure and  
571 processes governing persistent activity at Masaya Volcano, Nicaragua. Bull. Volcanol.  
572 59, 345-355.
- 573 Sable, J.E., Houghton, B.F., Wilson, C.J.N., Carey, R.J., 2006. Complex proximal  
574 sedimentation from Plinian plumes: the example of Tarawera 1886. Bull. Volcanol.  
575 69, 89-103.

- 576 Sarna-Wojcicki, A.M., Shipley, S., Waitt, J.R., Dzurisin, D., Wood, S.H., 1981. Areal  
577 distribution, thickness, mass, volume and grain-size of air-fall ash from the six major  
578 eruptions of 1980. U. S. Geol. Surv. Prof. Pap. 1250, 577- 600.
- 579 Sparks, R.S.J., Bursik, M.I., Ablay, G.J., Thomas, R.M.E., Carey, S.N., 1992. Sedimentation  
580 of tephra by volcanic plumes. Part 2: controls on thickness and grain-size variations of  
581 tephra fall deposits. Bull. Volcanol. 54, 685-695.
- 582 Stoiber, R.E., Williams, S.N., 1986. Sulfur and halogen gases at Masaya caldera complex,  
583 Nicaragua: Total flux and variations with time. J. Geophys. Res. 91, 12,215-12,231.
- 584 van den Bogaard, P., Schmincke, H.-U., 1984. The eruptive center of the Late Quaternary  
585 Laacher See Tephra. Geol. Rdsch. 73, 933-980.
- 586 van Wyk de Vries, B., 1993. Tectonics and magma evolution of Nicaraguan volcanic systems.  
587 Ph.D. Thesis. Open Univ., UK.
- 588 Walker, G.P.L., Self, S., Wilson, L., 1984. Tarawera 1886, New Zealand - A basaltic Plinian  
589 fissure eruption. J. Volcanol. Geotherm. Res. 21, 61-78.
- 590 Walker, J.A., Williams, S.N., Kalamarides, R.I., Feigenson, M.D., 1993. Shallow open-  
591 system evolution of basaltic magma beneath a subduction zone volcano: the Masaya  
592 Caldera Complex, Nicaragua. J. Volcanol. Geotherm. Res. 56, 379-400.
- 593 Wehrmann, H., Bonadonna, C.B., Freundt, A., Houghton, B.F., Kutterolf, S., 2006. A  
594 basaltic-andesitic plinian eruption revisited: case study of Fontana Tephra, Nicaragua.  
595 In: W.I. Rose, G.J.S. Bluth, M.J. Carr, J.W. Ewert, L.C. Patino, J.W. Vallance  
596 (Editors), Volcanic hazards in Central America. Geol. Soc. Am. Spec. Pap. 412, pp.  
597 209-223.
- 598 Wehrmann, H., 2005. Volatile degassing and Plinian eruption dynamics of the mafic Fontana  
599 Tephra, Nicaragua. Ph.D. Thesis. Kiel Univ., Germany.
- 600 Williams, S.N., 1983. Plinian airfall deposits of basaltic composition. Geology 11, 211-214.
- 601 Wilson, L., Walker, G.P.L., 1987. Explosive volcanic eruptions: VI. Ejecta dispersal in  
602 plinian eruptions: the control of eruption conditions and atmospheric properties.  
603 Geophys. J. R. Astron. Soc. 89, 657-679.
- 604 Woods, A.W., 1988. The fluid dynamics and thermodynamics of eruption columns. Bull.  
605 Volcanol. 50, 169-193.

606 **Figure Captions**

607

608 Figure 1: Digital elevation model of Nicaragua showing the two large lakes, the position of  
 609 the volcanic front and the location of the Masaya Caldera Complex. The black stippled line  
 610 marks the boundary of the Nicaraguan depression after van Wyk de Vries (1993).

611

612 Figure 2: Facies distribution of the Masaya Triple Layer, with La Concepción facies (LCF) to  
 613 the south of the caldera and the Managua facies (MF) to the northwest. The open circles and  
 614 squares represent the studied localities and the red lines connect the proximal profiles shown  
 615 in figures 4 and 7. Note the lack of MTL outcrops to the west (direction to El Crucero) and  
 616 northeast (towards Tipitapa).

617

618 Figure 3: End-member types of juvenile fragments of the Masaya Triple Layer in thin section:  
 619 [a] highly vesicular sideromelane (~80 vol. % porosity), [b] moderately vesicular tachylite  
 620 with ~40 vol. % round vesicles and [c] incipiently vesicular tachylite, where the vesicularity  
 621 consists of irregular-shaped voids (~16 vol. %).

622

623 Figure 4: Diagram SiO<sub>2</sub> vs. MgO comparing the composition of the two facies of the Masaya  
 624 Triple Layer (La Concepción facies -LCF- and Managua facies -MF- ) with the composition  
 625 fields of other major tephra units from Masaya caldera (SAT=San Antonio Tephra,  
 626 MT=Masaya Tuff, TIL=Ticuantepe Lapilli) and the older Las Sierras volcanic system  
 627 (FT=Fontana Tephra, LSF=Las Sierras Formation; data from Wehrmann (2005) and own  
 628 unpublished data).

629

630 Figure 5: Proximal stratigraphy of La Concepción facies, south of the caldera. The profile line  
 631 is shown in Fig. 2. Gray shading correlates lapilli beds between outcrops. Note the different  
 632 degrees of erosion at the top of the outcrops, with the Masaya Tuff lying unconformably  
 633 above.

634

635 Figure 6: Photographs of the juvenile particles of layer B5. [a] Selected particles with fluidal  
 636 shapes and glassy surfaces. [b] Whole deposit as it looks in the outcrops. [c] Highly vesicular  
 637 brown sideromelane glass in thin section.

638

639 Figure 7: Photographs of the tuff sequence B6-B10 with intercalated well-sorted fall deposits.  
 640 [a] At an outcrop 3 km S from the caldera rim where the layers are several cm thick. [b] The  
 641 three tuffs at 7.5 km S of the caldera rim.

642

643 Figure 8: Stratigraphy of the Managua facies at the most proximal exposures NW of the  
 644 caldera. The profile line and location of the outcrops are shown in Fig. 2. Correlations  
 645 between outcrops are indicated by gray shading.

646

647 Figure 9: Variation diagrams showing the complete overlap in: [a] major element (FeO vs.  
 648 MgO) and [b] trace-element (Ba vs. Zr) compositions of matrix glass, [c] Al<sub>2</sub>O<sub>3</sub> vs. CaO  
 649 concentrations of melt inclusion glasses, and [d] K<sub>2</sub>O vs. CaO concentrations in plagioclase  
 650 phenocrysts from the Managua facies (MF) and La Concepción facies (LCF).

651

652 Figure 10: Proposed correlation between La Concepción and the Managua facies based on the  
 653 marker beds B5 and C2 (subunit II, correlation in red). As indicated, the left profile -MF- is  
 654 towards the NW of the caldera and the right profile -LCF- is to the S of Masaya caldera.

655

656 Figure 11: Isopach maps for the main fallout subunits I, II, III, IV, VI, X and the surge-tuff  
657 subunits V, VII and IX of the Masaya Triple Layer. Isopach contours are in cm and the  
658 dashed lines are estimated in areas with no data. The cities of Managua and Masaya are  
659 shown in gray.

660

661 Figure 12: Diagram of isopach thickness vs. square root of isopach area for the MTL fallout  
662 subunits. The fields of Plinian, Subplinian and Phreatoplinian eruptions are from Houghton et  
663 al. (2000). The inset at the top right corner shows the same diagram on a bigger scale for the  
664 entire MTL including the thickness data from the distal marine tephra layers.

665

666 Figure 13: Crosswind range versus maximum downwind range of the MP and ML isopleths  
667 for subunits II, III, IV, VI and X of the MTL. The model curves are from Carey and Sparks  
668 (1986). Most of the MTL data locate between 20 and 28 km column height and indicate  
669 different winds speeds for the subunits.

670

671 Figure 14: Eruption column height versus log of the mass eruption rate with the lines for  
672 different eruption temperatures of Woods (1988). The colored oval areas locate column  
673 heights for the fallout subunits II, III, IV, VI and X on the 1200 K line (eruption temperature  
674 for basaltic magmas). The eruption temperature of the poorly phyric basaltic MTL magma  
675 was probably 200 degrees higher such that mass eruption rates estimated from this figure are  
676 maximum estimates.

677

678 Figure 15: Isopachs in centimeters (dotted line) for the Masaya Triple Layer total thickness.  
679 The cross-circle symbols give the location of sediment gravity cores drilled offshore  
680 Nicaragua; labels indicate the core number and the thickness of the ash layer.

681

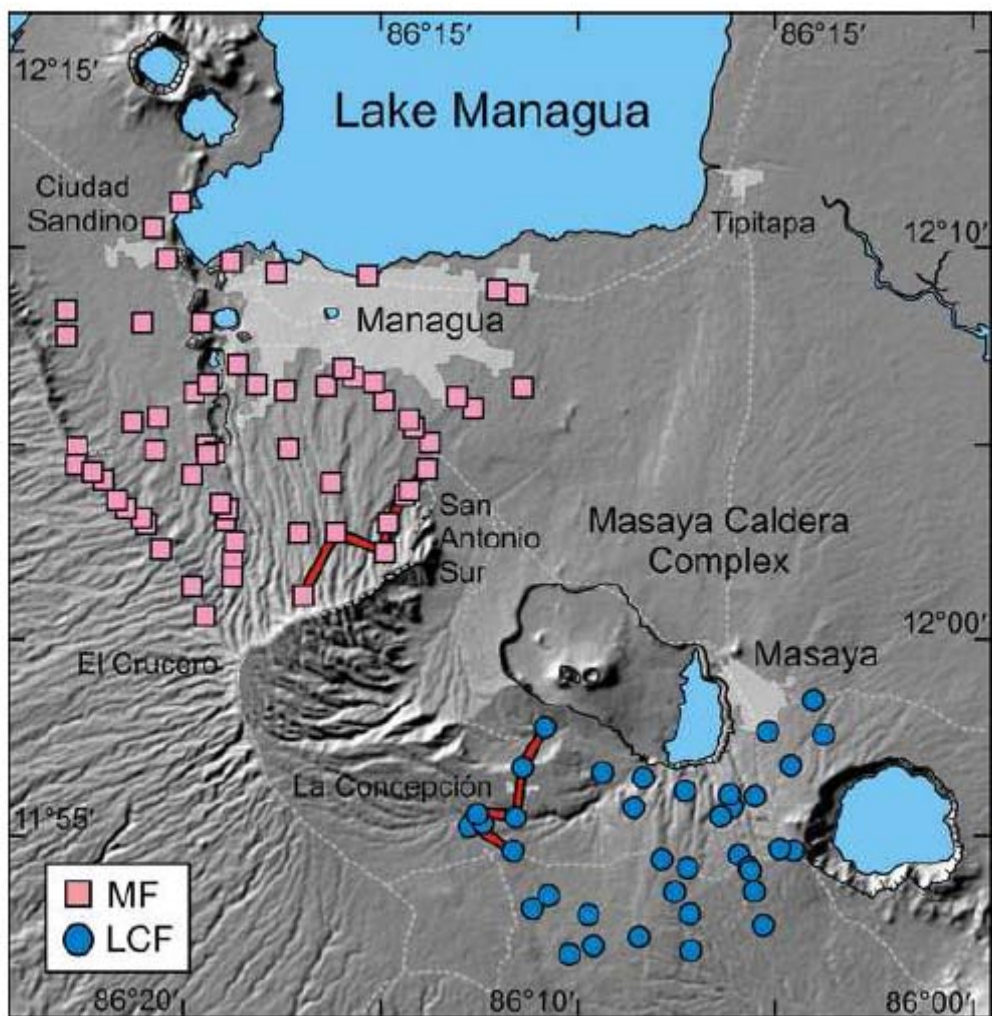
682 Figure 16. Schematic model of the Masaya Triple Layer eruption as discussed in the text,  
683 showing the main Plinian and Phreatoplinian eruptions interrupted by surge-forming  
684 phreatomagmatic activity. Blue lenses represent ground water accessing the conduit.

685 Fig 1  
686



687

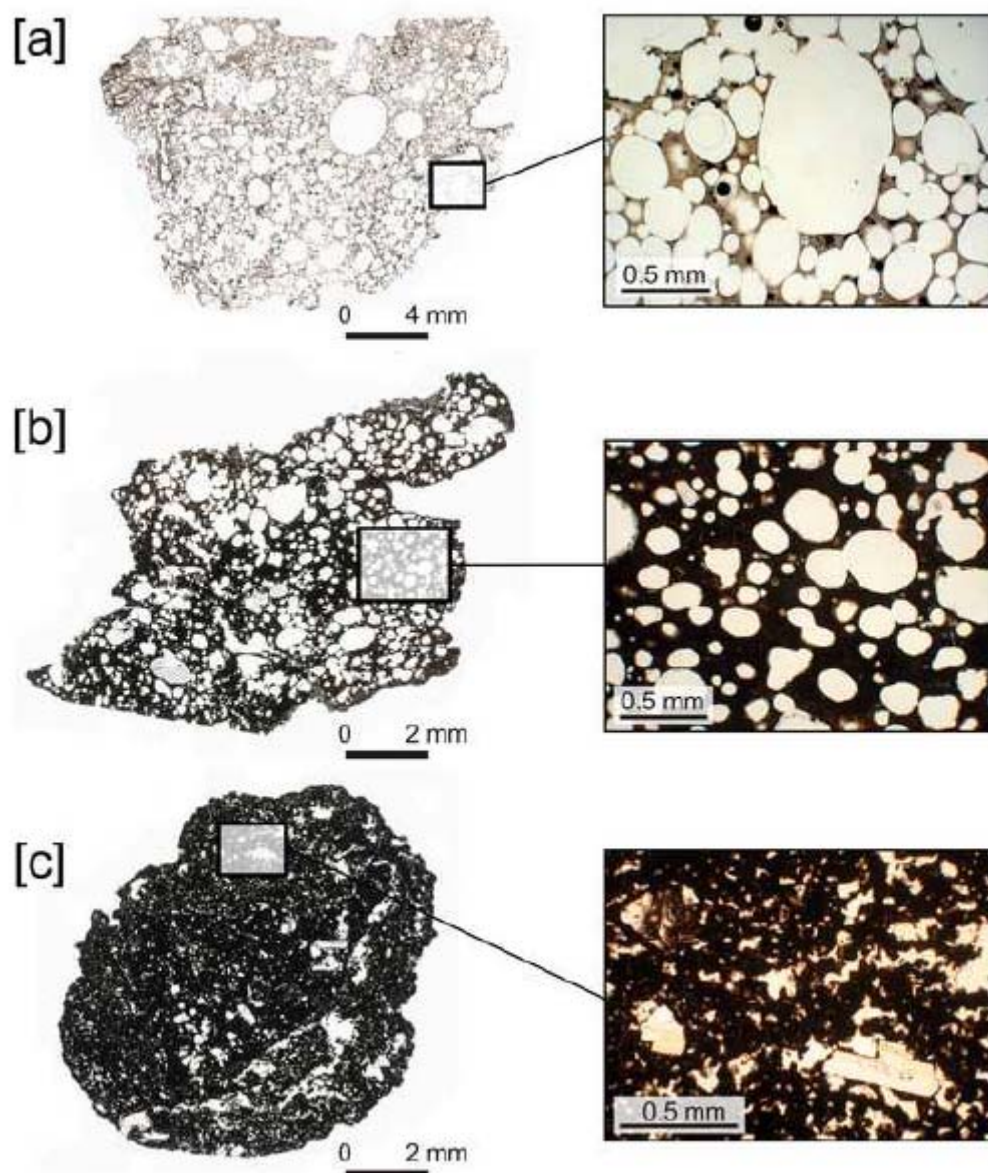
688 Fig 2  
689



690

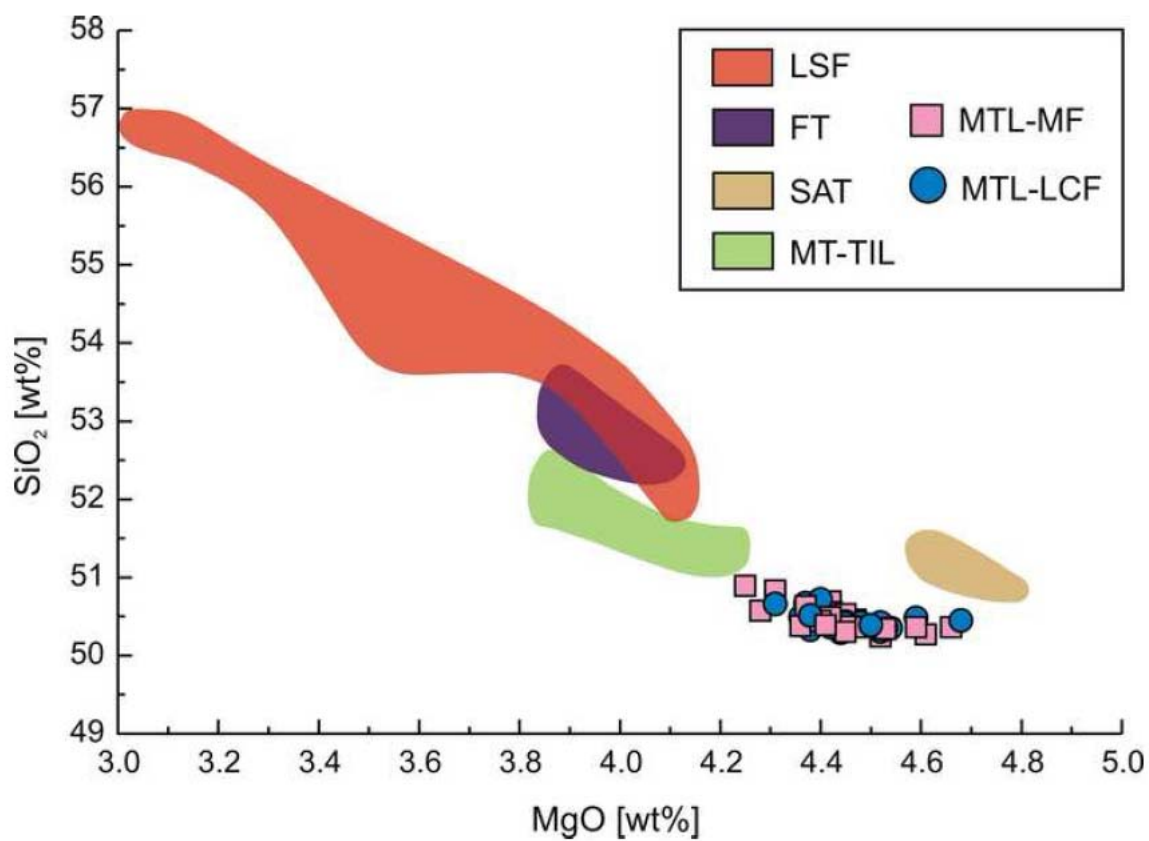
A

691 Fig 3  
692



693

694 Fig 4  
695

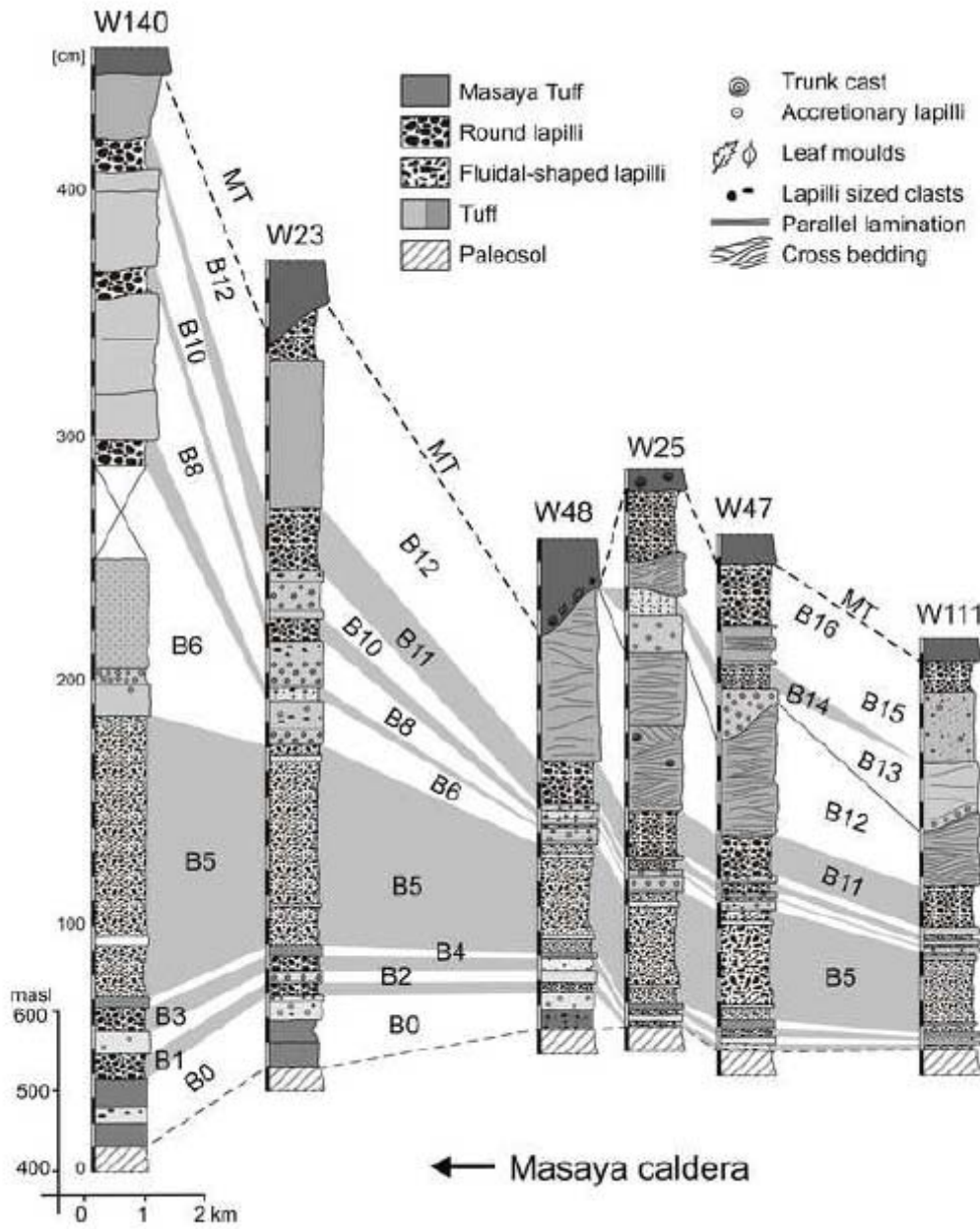


696

ACCEPTED

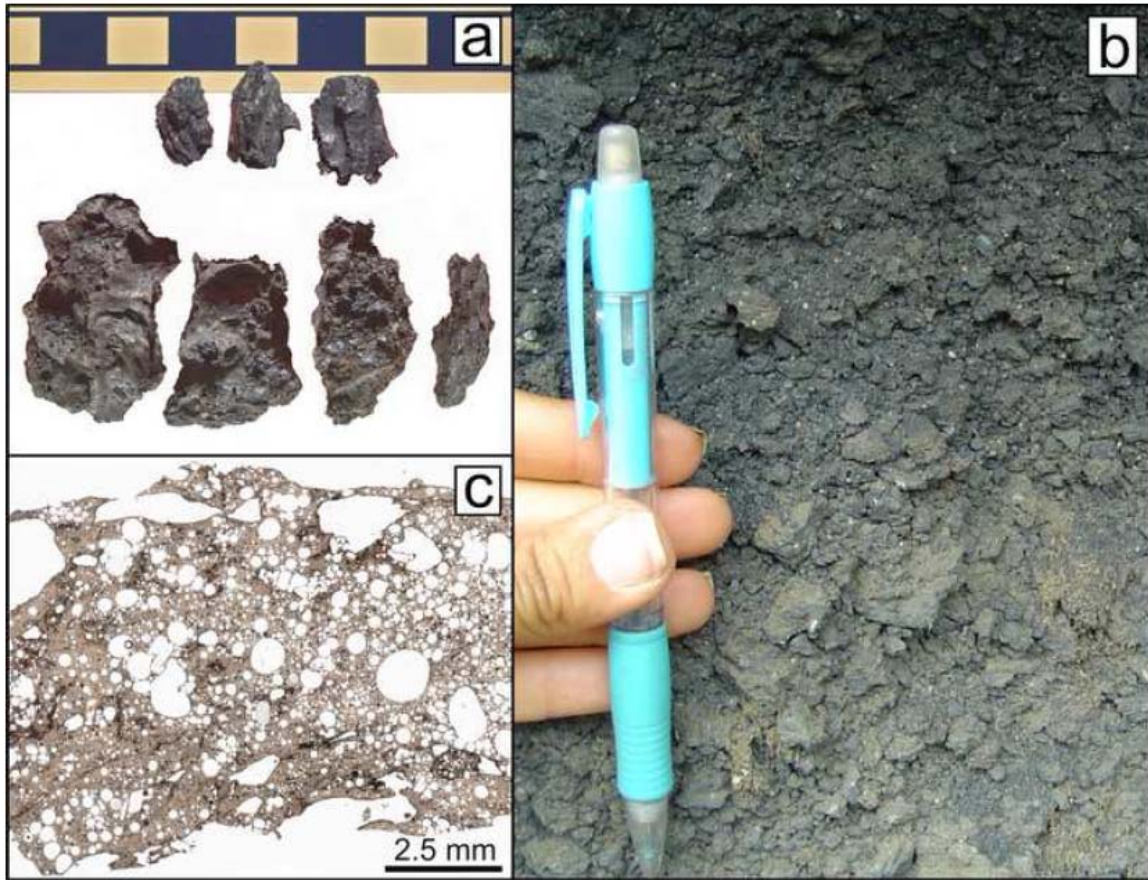


697 Fig 5  
698



699

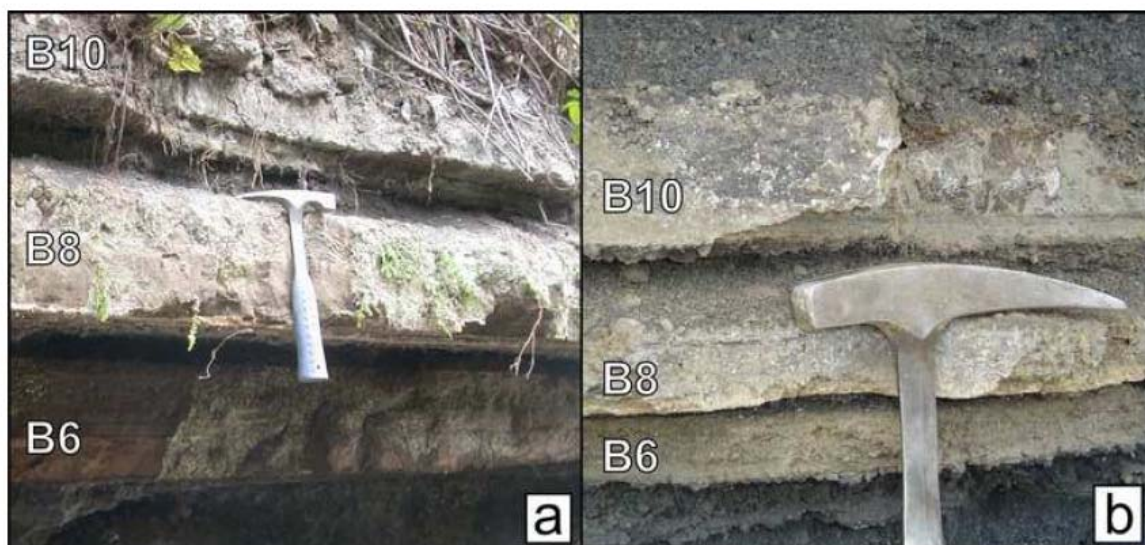
700 Fig 6  
701



702

ACCEP

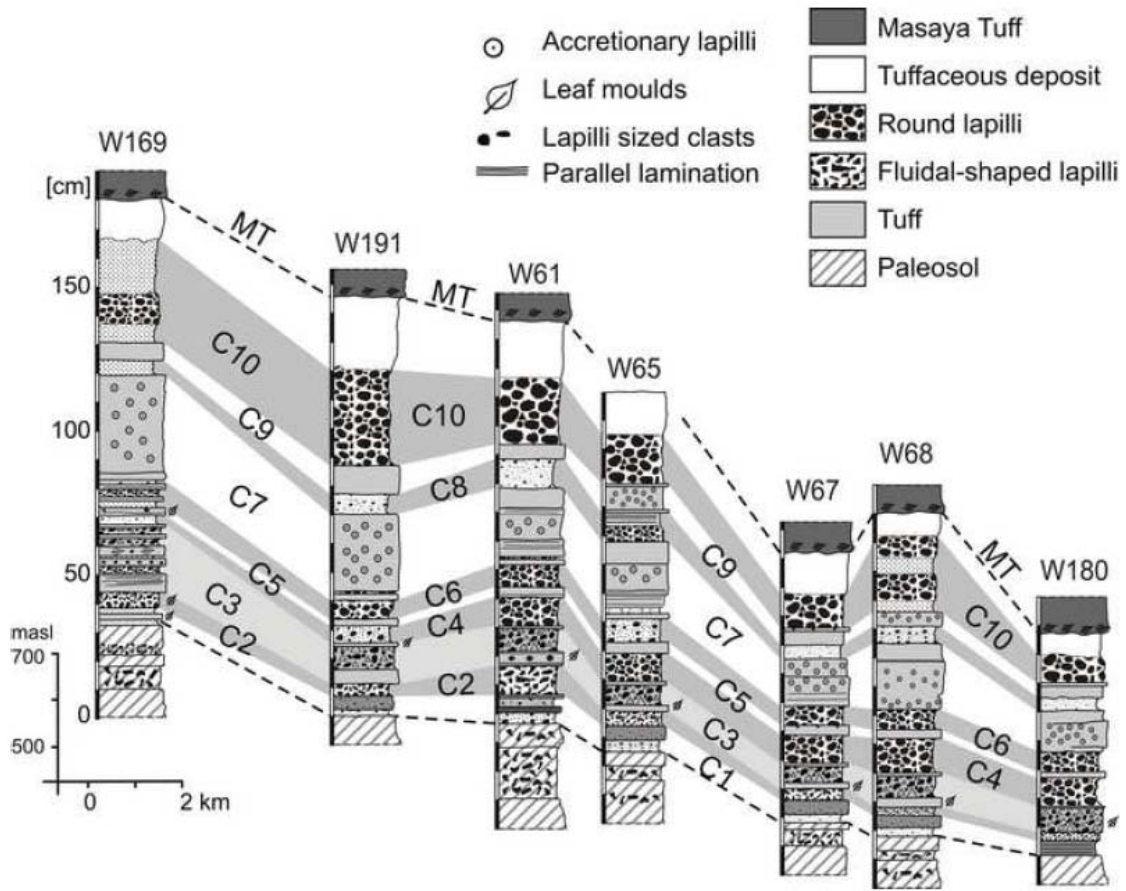
703 Fig 7  
704



705

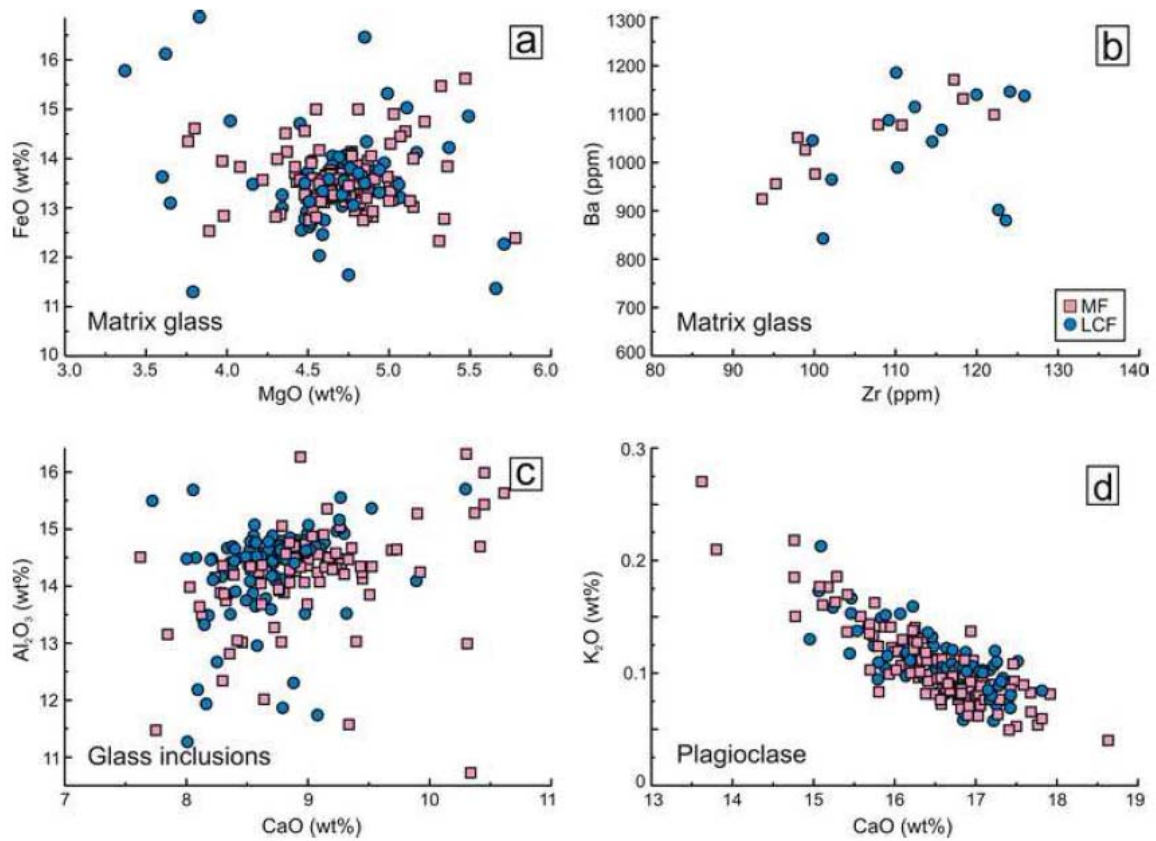
ACCEPTEL

706 Fig 8  
707



708

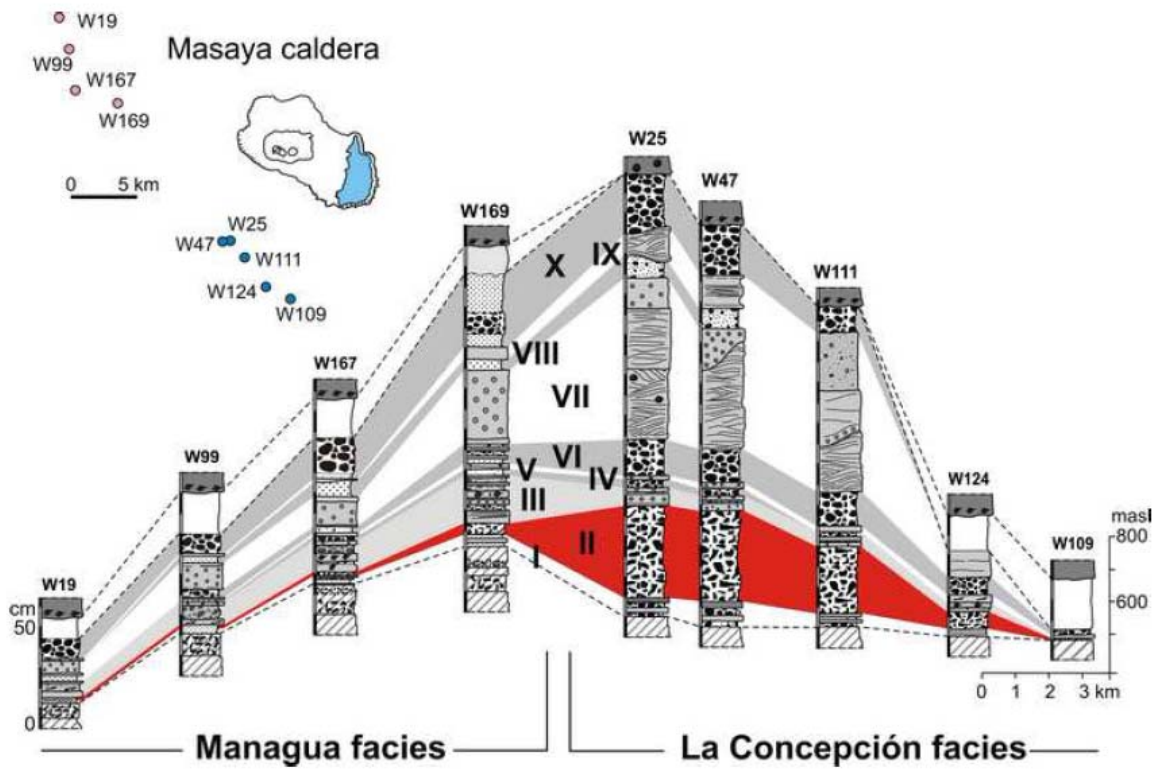
709 Fig 9  
710



711

ACCEPTED

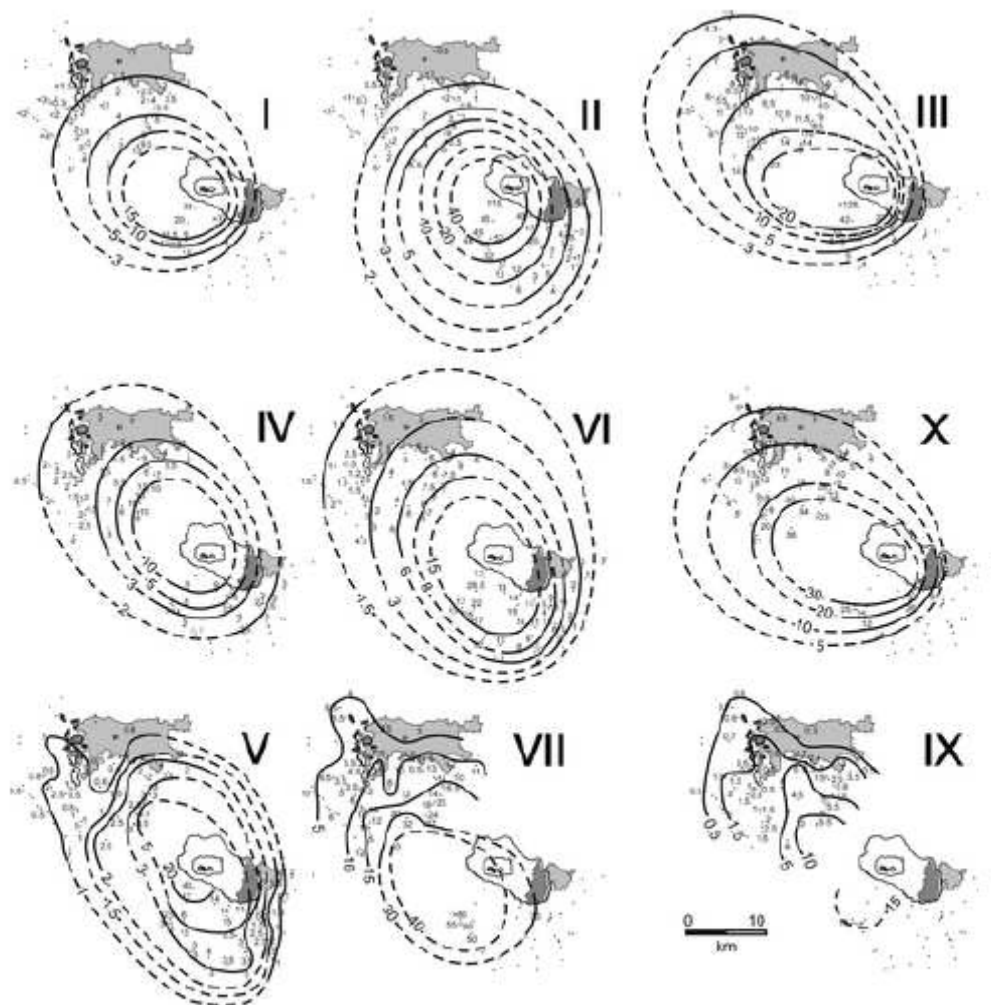
712 Fig 10  
713



714

ACCEPTED

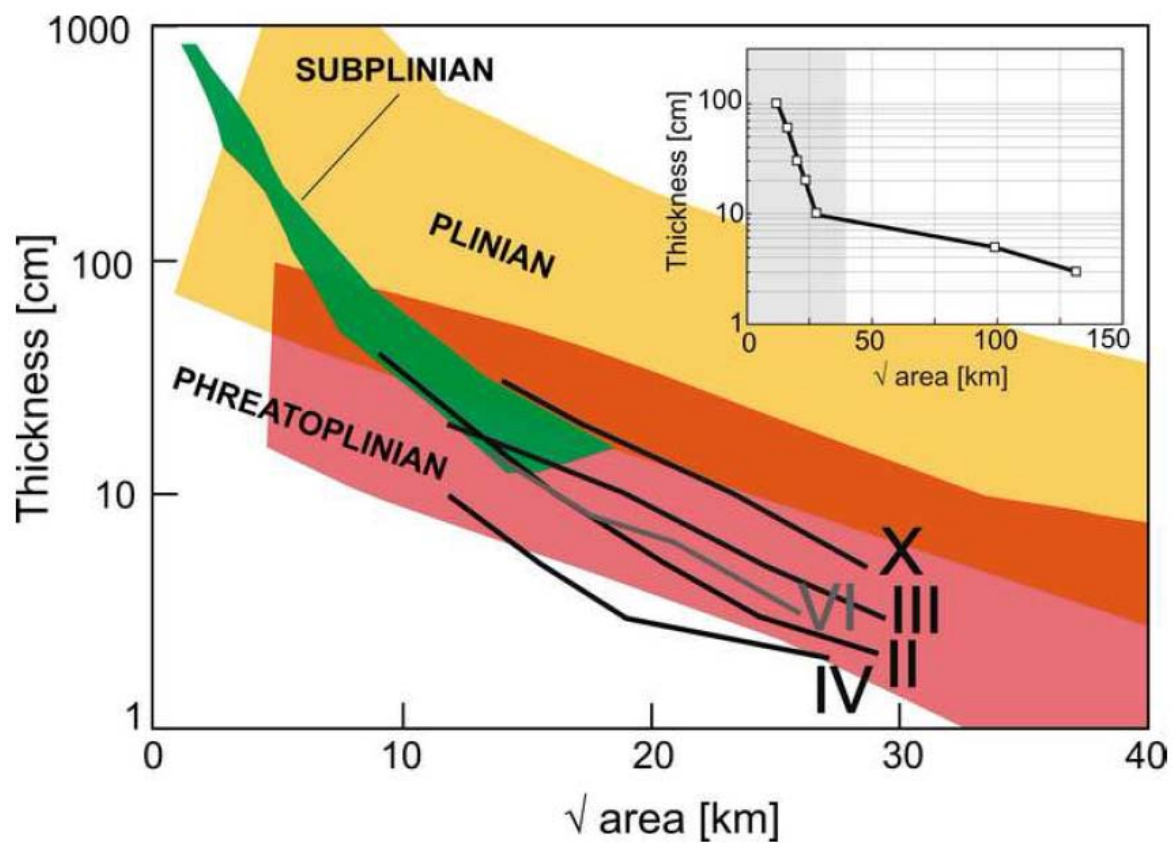
715 Fig 11  
716



717

A

718 Fig 12  
719

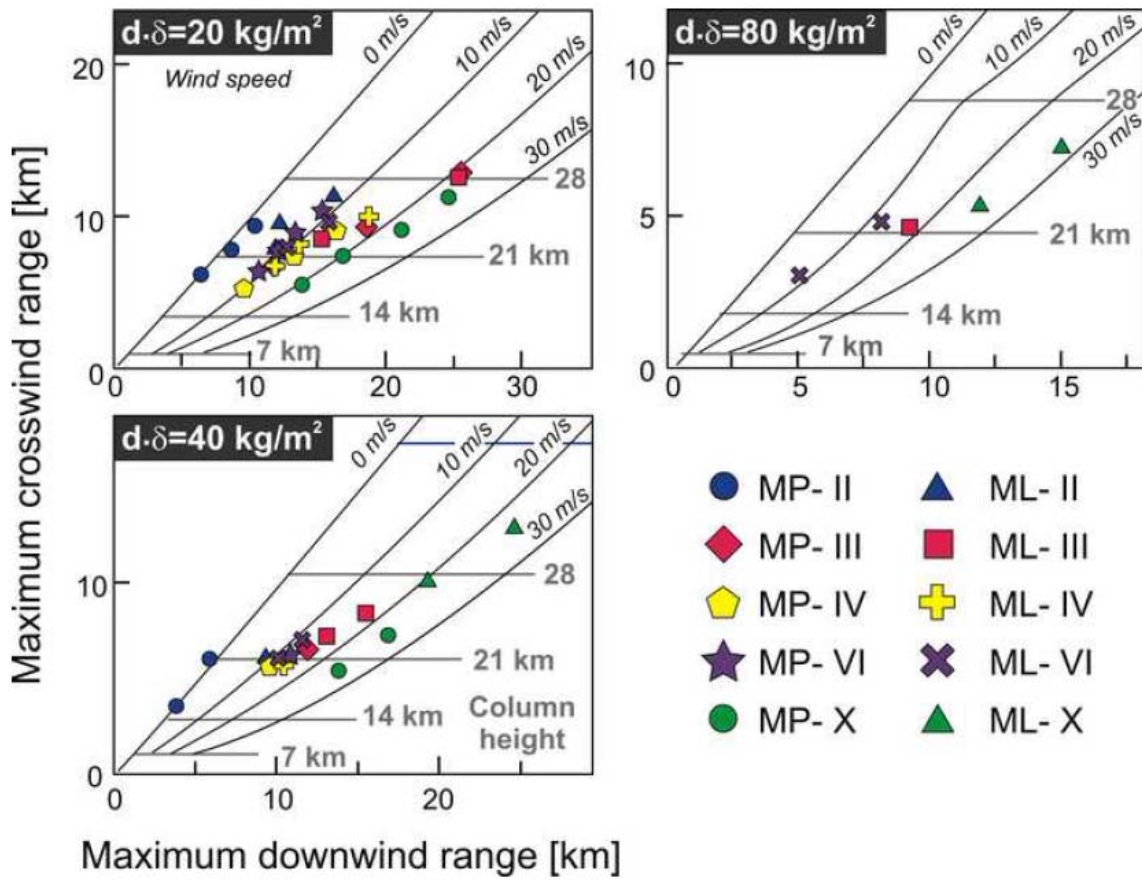


720

ACCEPTED

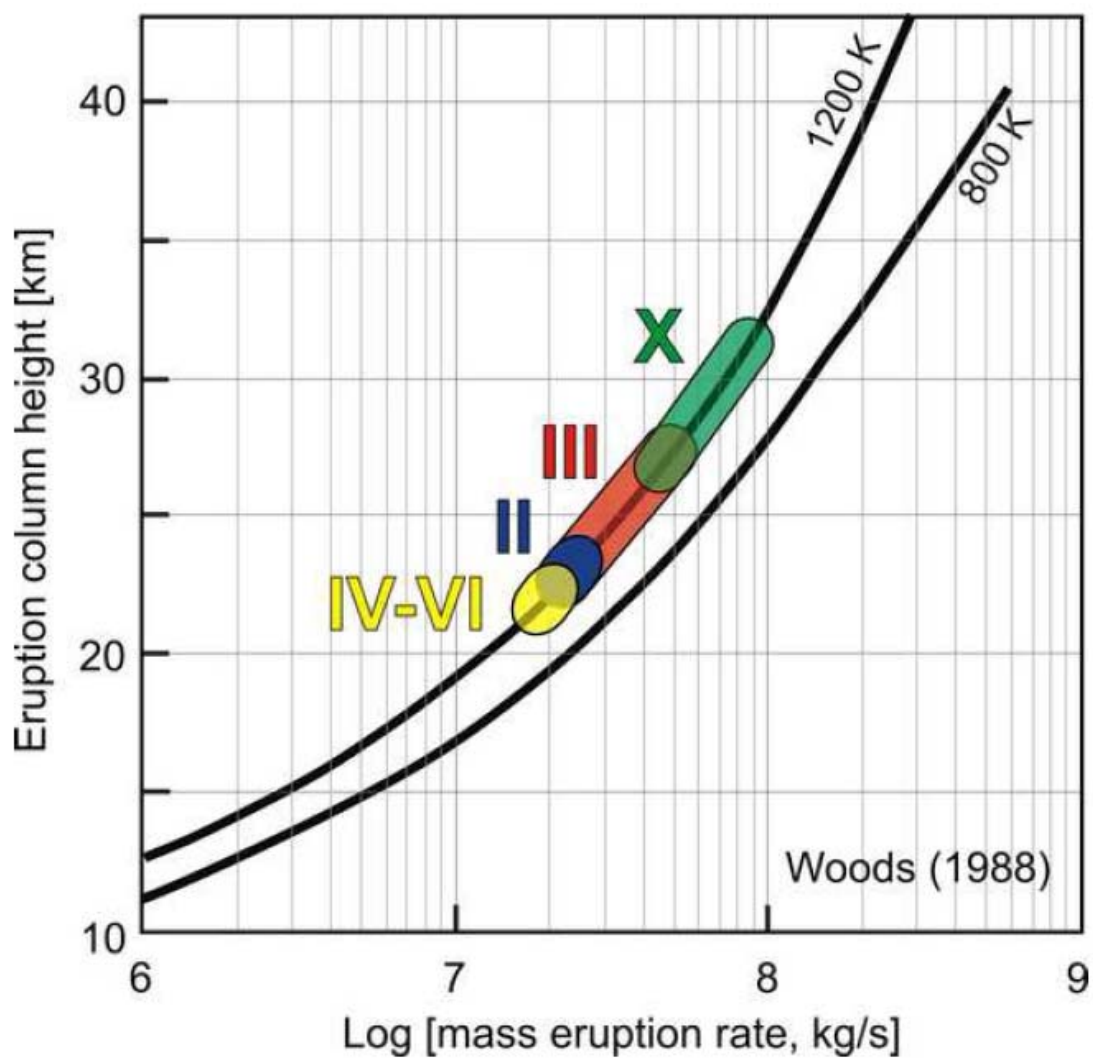


721 Fig 13  
722



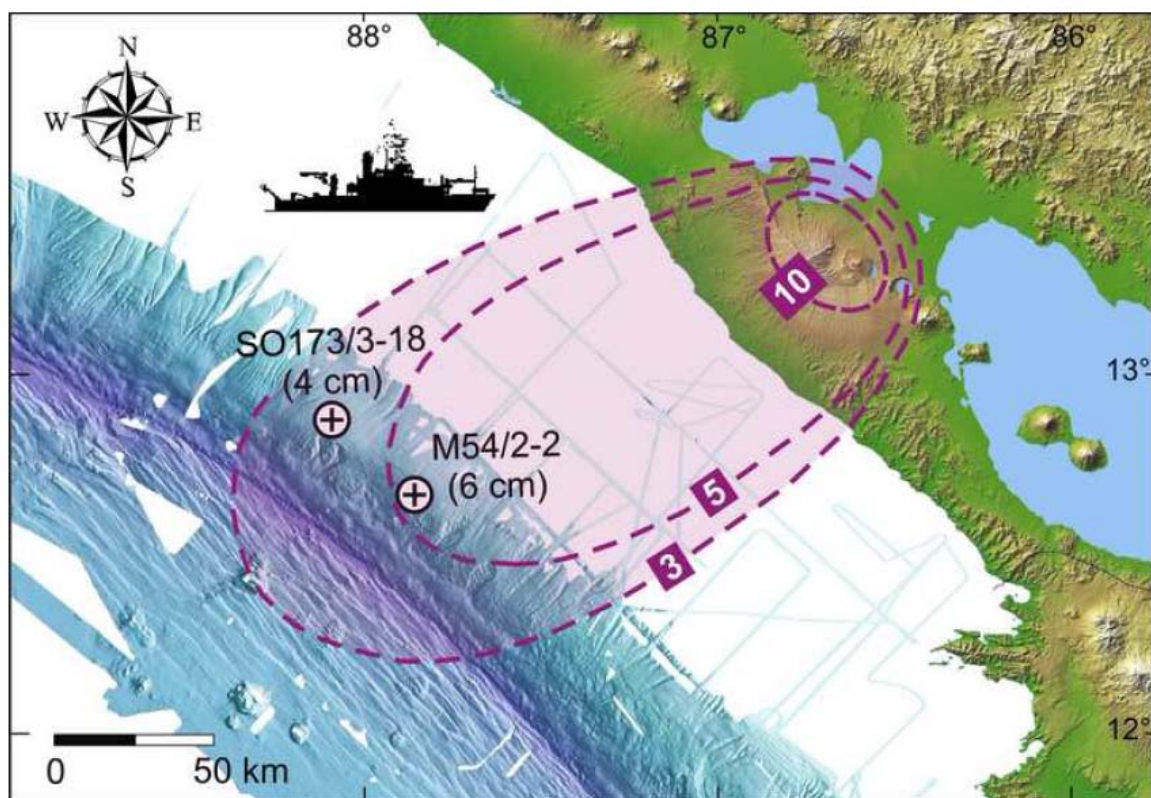
723

724 Fig 14  
725



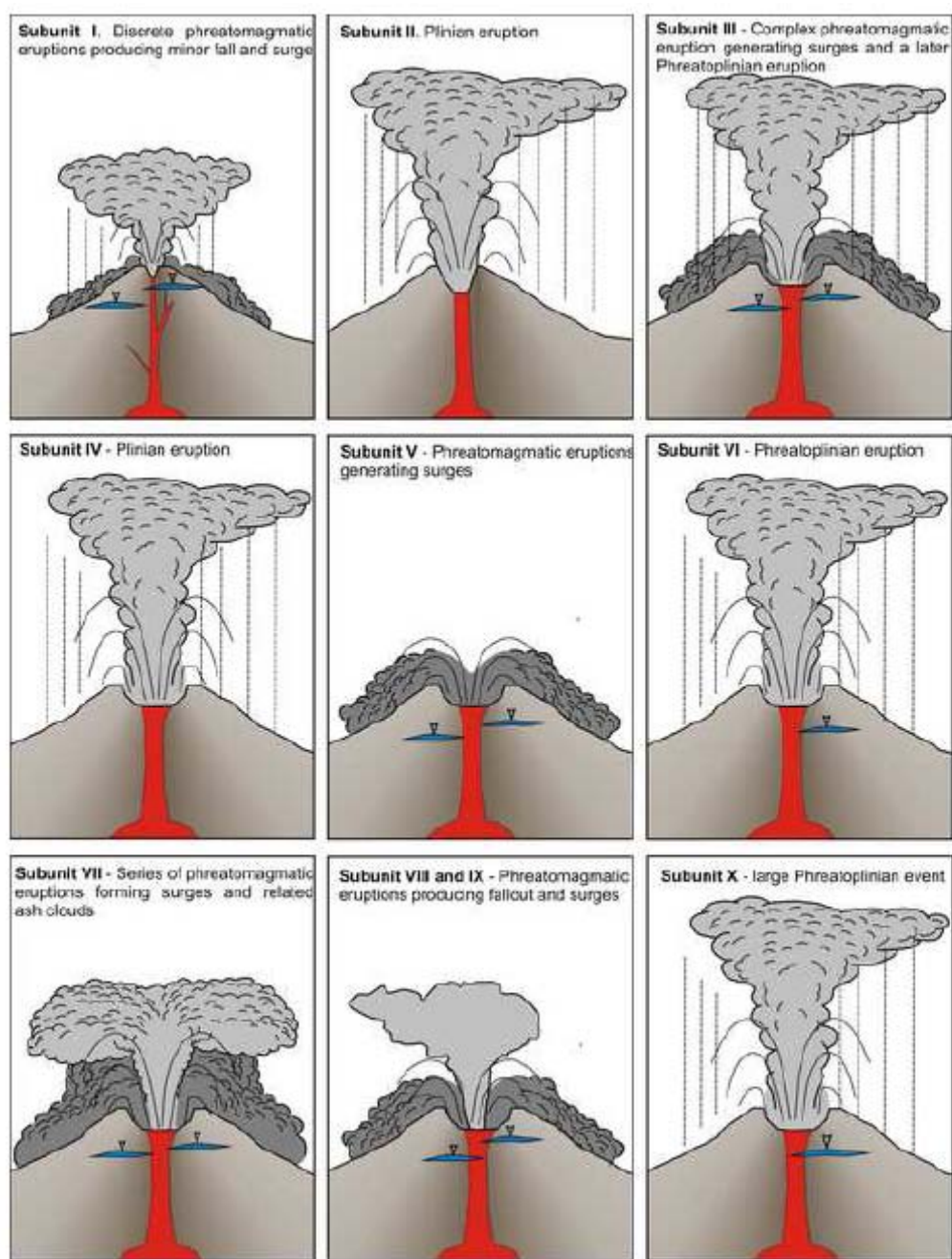
726

727 Fig 15  
728



729

730 Fig 16  
731



732

**Table 1.** Characteristics of the subunits of La Concepción facies. Most sorting values were estimated in the field but are supported by selected grain-size analyses. Vesicularity estimated in thin sections and calculated from measured clast bulk densities. ND means “not determined”.

Correl. subunit	LCF Subunit	Type of deposit	Sorting	Juvenile fragments	Density (g/cm <sup>3</sup> )	Vesicularity (vol.%)	Type of glass	Lithic fragments (vol.%, type)
	<b>B0</b>	Two basal loose fine ash layers and an indurated tuff at the top with accretionary lapilli and plant remains. Present only in proximal areas						
<b>I</b>	<b>B1</b>	Scoria lapilli	$\sigma \sim 1.5$	Incipiently to moderately vesicular lapilli, round, bread-crust shaped	0.8-1.35	7-17 40-50	Tachylite	~5 vol.%, hydrothermally altered lavas, plutonics,
	<b>B2</b>	Yellowish faintly laminated indurated fine tuff containing very fine accretionary lapilli and molds of grass leaves						
	<b>B3</b>	Fine scoria lapilli	$\sigma \sim 1.5$	Poorly to incipiently vesicular lapilli, round shaped	~1.5	ND	ND	1-2 vol.%, mostly hydrothermally altered
	<b>B4</b>	Laminated weakly-cemented tuff with coarse-ash base to very fine top. Consists mostly of poorly to non-vesicular glass shards and a minor fraction (~3-5 vol.%) of highly vesicular achnelith-shaped fragments. Load structures locally disturb the parallel lamination.						
<b>II</b>	<b>B5</b>	Scoria lapilli	$\sigma \sim 1$	Glassy, fluidal-shaped achneliths	0.25-1	45-80	Sideromelane	<<1 vol.%, small, hydrothermally altered
	<b>B6</b>	Grayish indurated tuff with a fine-grained lower part containing accretionary lapilli and a cross-bedded top of fine lapilli to coarse ash						
<b>III</b>	<b>B7</b>	Scoria fine lapilli to coarse ash	$\sigma \sim 1.5-2$	Moderately vesicular lapilli, ~5-10 vol.% poorly to incipiently vesicular	0.9-1 ~1.5	50-60	Sideromelane and tachylite	<1 vol.% some hydrothermally altered
	<b>B8</b>	Indurated tuff showing dune structures and cross bedding at proximal facies; accretionary lapilli-rich tuff at medial-distal facies						
<b>IV</b>	<b>B9</b>	Scoria lapilli, some ash coated	$\sigma \sim 1.5$	~90 vol.% incipiently vesicular, ~10 vol.% moderately vesicular	1.20-1.35 0.9-1.1	~18 40-44	Sideromelane, tachylite, mingled	~1 vol.% lava, mostly reddish altered
<b>V</b>	<b>B10</b>	Indurated grayish tuff, coarser and showing dunes and cross bedding at proximal areas, at distal is fine-grained with accretionary lapilli						
<b>VI</b>	<b>B11</b>	Scoria lapilli	$\sigma \sim 1.7-2$	Moderately - poorly vesicular lapilli, incipiently vesicular lapilli, ~20 vol.% moderately vesicular	~0.8 1.2-1.6 ~0.65	17-20 30-45	Tachylite, minor sideromelane	~3-5 vol.% vesicular lava, plutonics, reddish lithics
<b>VII</b>	<b>B12</b>	Two indurated tuff beds, the lowermost of lapilli and coarse-ash with cross-bedding and dune structures containing plant molds, the upper one is finer-grained (ash) with low-angle cross-bedding. Contains armored lapilli with lava and scoria cores.						
	<b>B13</b>	Grayish accretionary lapilli-rich fine tuff containing dispersed scoria lapilli.						
<b>VIII</b>	<b>B14</b>	Lapilli to coarse ash, faint cross-bedding	$\sigma \sim 2.5$	Poorly to moderately vesicular, incipiently vesicular lapilli, coated with fine ash	ND	35-50 ~8	Tachylite	ND
<b>IX</b>	<b>B15</b>	Gray to yellowish indurated fine tuff with scattered accretionary lapilli, cross-bedding and lapilli-rich lenses						
<b>X</b>	<b>B16</b>	Scoria lapilli	$\sigma \sim 2$	~80 vol.% moderately vesicular, ~15 vol.% highly vesicular, ~5 vol.% dense	~0.4, 0.6-0.7, 1.1-1.5	20-30	Tachylite	~5 vol.% basaltic lavas, some hydrothermally altered

**Table 2.** Characteristics of the subunits of the Managua facies. Most sorting values were estimated in the field but are supported by selected grain-size analyses. Vesicularity estimated in thin sections and calculated from measured clast bulk densities. ND means “not determined”.

Correl. subunit	MF Subunit	Type of deposit	Sorting	Juvenile fragments	Density (g/cm <sup>3</sup> )	Vesicularity (vol.%)	Type of glass	Lithic fragments (vol.%, type)
I	C1	a	$\sigma \sim 1.5$	Highly to moderately vesicular scoria lapilli to coarse ash	0.6-1.1	ND	Sideromelane	<1 vol.%, reddish small lithics
		b						
II	C2	Scoria fine-lapilli	$\sigma \sim 1-1.3$	Moderately to highly vesicular fluidal glassy scoria	$\sim 0.6$ 0.9-1.1	$\sim 70$ 30-40	Sideromelane	<1 vol.%
III	C3	Normal-graded scoria lapilli layer with 30 vol.% of ash, sandwiched by thin tuffs	$\sigma \sim 2-2.5$	Mostly round poorly vesicular scoria, minor moderately to poorly vesicular scoria lapilli, mostly coated with fine ash	1.8-2.3 $\sim 1.3$	<40 45-65	Mixture of sideromelane and tachylite	$\sim 5-15$ vol.%, angular aphyric hydrothermally altered lava
IV	C4	Slightly normal-graded scoria lapilli layer	$\sigma \sim 1.5$	Highly vesicular scoria and minor denser juveniles	0.6-0.8 $\sim 1.3$	40-50	Tachylite and lesser vesicular sideromelane	<3 vol.%, basaltic lava fragments
V	C5	Indurated yellowish thin tuff, with desiccation cracks at the top and showing a lower cross-bedded portion and leaf molds at proximal outcrops						
VI	C6	Scoria lapilli	$\sigma \sim 1.8-2$	Mostly highly vesicular glassy light scoria lapilli, but also moderately vesicular and dense	0.6-0.9 $\sim 1.3$	10-40	Tachylite, sideromelane at the rims	<5 vol.%, mostly hydrothermally altered
VII	C7	Thick yellowish tuff with abundant accretionary lapilli and crude internal stratification, massive or planar bedded						
VIII	C8	Coarse ash and few lapilli	$\sigma \sim 2.2$	Moderately to poorly vesicular fine lapilli and dense coarse to fine ash	0.7-1.1	>12	Tachylite, minor sideromelane	$\sim 2$ vol.%, hydrothermally altered fragments
IX	C9	Indurated fine tuff with accretionary lapilli and small floating lapilli fragments, at the top a thin hardened level with desiccation cracks						
X	C10	Reverse-graded scoria lapilli	$\sigma \sim 1.8-2$	Moderately to poorly vesicular lapilli and small fraction of highly vesicular scoria lapilli	1.3-1.7 0.8-0.9	30-60	Tachylite, minor sideromelane	$\sim 5$ vol.%, mostly hydrothermally altered basaltic lava

**Table 3.** Volume and eruption parameters calculated for the subunits I-X

Subunit	Volume (km <sup>3</sup> )		Column height (km)	Wind speed (m/s)	Mass flux (kg/s)
	Bulk	DRE			
I	0.068	0.028			
II	0.115	0.038	~22-24	<2	10 <sup>7</sup> -10 <sup>8</sup>
III	0.125	0.102	~22-28	~10	10 <sup>6</sup> -10 <sup>7</sup>
IV	0.052	0.025	~21-23	~10	10 <sup>6</sup> -10 <sup>7</sup>
V	0.037	0.015			
VI	0.099	0.038	~21-23	~10	10 <sup>6</sup> -10 <sup>7</sup>
VII	0.018	0.007			
VIII	0.076	0.030			
IX	0.046	0.018			
X	0.219	0.115	~26-32	~20	10 <sup>6</sup> -10 <sup>7</sup>